

An Annual Cycle of Submesoscale Vertical Flow and Restratification in the Upper Ocean



Xiaolong Yu*, Alberto C. Naveira Garabato

Department of Ocean and Earth Sciences, University of Southampton, UK

Adrian P. Martin

National Oceanography Centre, Southampton, UK

Christian E. Buckingham

Univ. Brest, CNRS, IRD, Ifremer, Laboratoire d'Océanographie Physique et Spatiale

(LOPS), IUEM, Brest, France

Liam Brannigan

Department of Meteorology, Stockholm University, Stockholm, Sweden

Zhan Su

Environmental Science and Engineering, California Institute of Technology, USA

*Current affiliation: Ifremer, Univ. Brest, CNRS, IRD, Laboratoire d'Océanographie Physique et Spatiale (LOPS), IUEM, Brest, France.

Corresponding author: Xiaolong Yu, xiaolong.yu@ifremer.fr

Early Online Release: This preliminary version has been accepted for publication in *Journal of the Physical Oceanography*, may be fully cited, and has been assigned DOI 10.1175/JPO-D-18-0253.1. The final typeset copyedited article will replace the EOR at the above DOI when it is published.

Abstract

Numerical simulations suggest that submesoscale turbulence may transform lateral buoyancy gradients into vertical stratification, and thus restratify the upper ocean via vertical flow. However, the observational evidence for this restratifying process has been lacking due to the difficulty in measuring such ephemeral phenomena, particularly over periods of months to years. This study presents an annual cycle of the vertical velocity and associated restratification estimated from two nested clusters of meso- and submesoscale-resolving moorings, deployed in a typical mid-ocean area of the Northeast Atlantic. Vertical velocities inferred using the non-diffusive density equation are substantially stronger at submesoscales (horizontal scales of 1-10 km) than at mesoscales (horizontal scales of 10-100 km), with respective root mean square values of 38.0 ± 6.9 m/day and 22.5 ± 3.3 m/day. The largest submesoscale vertical velocities and rates of restratification occur in events of a few days' duration in winter and spring, and extend down to at least 200 m below the mixed layer base. These events commonly coincide with the enhancement of submesoscale lateral buoyancy gradients, which is itself associated with persistent mesoscale frontogenesis. This suggests that mesoscale frontogenesis is a regular precursor of the submesoscale turbulence that restratifies the upper ocean. The upper-ocean restratification induced by submesoscale motions integrated over the annual cycle is comparable in magnitude to the net destratification driven by local atmospheric cooling, indicating that submesoscale flows play a significant role in determining the climatological upper-ocean stratification in the study area.

1. Introduction

Vertical flows in the ocean surface boundary layer play a key role in shaping upper-ocean stratification, and in exchanging mass and tracers within and across the mixed layer (ML) (Klein and Lapeyre 2009; Rosso et al. 2014; Mahadevan 2016; McWilliams 2016). Oceanic submesoscale processes (defined here as those linked to subinertial flows with horizontal scales of 1-10 km) have been shown, mostly through numerical simulations, to be effective at inducing strong vertical velocities in the upper ocean (Mahadevan and Tandon 2006; Capet et al. 2008a). The occurrence of vertical motion at submesoscales is associated with a wide range of mechanisms characterised by distinct dynamics, such as surface frontogenesis (Lapeyre et al. 2006; Capet et al. 2008b; Gula et al. 2014), ML baroclinic instabilities (Boccaletti et al. 2007; Fox-Kemper et al. 2008), wind-driven frictional effects at fronts (Thomas and Lee 2005; Thomas and Ferrari 2008), nonlinear Ekman pumping (Thomas and Rhines 2002; Mahadevan et al. 2008), symmetric instability (Taylor and Ferrari 2010; Thomas et al. 2013; Brannigan 2016) and mesoscale-submesoscale coupling (Ramachandran et al. 2014). Most of the aforementioned studies have focused on regions of strong frontal currents or have made use of idealised simulations, while less attention has been devoted to investigating submesoscale flows in the open ocean (e.g., Shcherbina et al. 2015; Thompson et al. 2016) – which constitutes the majority of the marine environment.

The generation of submesoscale motions has been extensively documented in the ML, where the weak local stratification permits the rapid amplification of baroclinically unstable modes (Haine and Marshall 1998). In contrast, balanced flow in the ocean interior is commonly considered to follow quasi-geostrophic (QG) dynamics, characterized by mesoscale motions with horizontal scales of 10-100 km

(approaching or exceeding the first baroclinic deformation radius) and vertical scales of $O(1 \text{ km})$. These balanced interior flows are often generated by mesoscale baroclinic instability (BCI) (Gill et al. 1974), whereby slumping of isopycnals unfolds over relatively long time scales on the order of weeks to months (Charney 1971). Compared to mesoscale BCI in the interior, BCI in the ML develops over substantially smaller horizontal scales (1-10 km) and shorter time scales of order 1 day (Boccaletti et al. 2007). Both numerical simulations and observations indicate that variations in the intensity of mixed-layer BCI play a significant role in the seasonal modulation of submesoscale flows in the upper ocean (Mensa et al. 2013; Sasaki et al. 2014; Callies et al. 2015, 2016). Mixed-layer BCI has been parameterised as an overturning streamfunction confined to the ML (Fox-Kemper et al. 2008), acting to rapidly restratify the upper ocean by releasing available potential energy. Simulations by Callies et al. (2016) indicate that mixed-layer BCI may energise the entire ML and produce intense vertical velocities. In contrast, the impact of balanced submesoscale motions with characteristic horizontal scales of 1-10 km on interior vertical flows remains relatively understudied, although several recent numerical investigations suggest that these flows may play an important role in vertical exchanges across and below the ML base (e.g., Brannigan 2016).

A common outcome of the development of mesoscale BCI in the ML is the occurrence of frontogenesis, which is associated with large vertical velocities (Spall 1995; McWilliams et al. 2009). The connection between frontogenesis and restratification was established in the classical work of Hoskins and Bretherton (1972), who show that, in the presence of a larger-scale strain flow, an ageostrophic secondary circulation leads to buoyancy and momentum transports that maintain thermal wind balance. In the frontogenetic scenario, this ageostrophic secondary

circulation gradually slumps isopycnals and restratifies the upper ocean (i.e. it elicits an upward buoyancy flux). Thomas and Ferrari (2008) suggest that frontogenesis can penetrate from the ocean surface to depths beyond the ML base in the presence of deep fronts. Here, we will show that submesoscale vertical flows can be associated with strong mesoscale frontogenesis, which leads to substantial upper-ocean restratification down to at least 200 m below the ML base.

A key step in advancing our understanding of submesoscale turbulence and its associated restratification is to obtain representative observations of these phenomena in the upper ocean. However, due to the small magnitude of the vertical flows involved, the effects of submesoscale motions on stratification are difficult to measure directly. For several decades, the QG omega equation and variants have been widely used to estimate the vertical velocity for mesoscale flows (Pollard and Regier 1992; Martin and Richards 2001; Naveira Garabato et al. 2001; Thomas and Joyce 2010). At the submesoscale, ageostrophic motions are increasingly important, and the QG approximation provides a sub-optimal representation of the dynamics governing the vertical flow (Mahadevan 2016). An inverse formulation recently developed by Thomas et al. (2010) offers a dynamically comprehensive diagnostic of submesoscale vertical velocity from Seasoar data, but relies on the measurement of an assortment of spatial gradients and on specific assumptions about the character of temporal variability.

An alternative approach, based on the density conservation equation, has been successfully applied to oceanographic mooring observations. Previous research has pursued this method to estimate vertical velocity from individual moorings under the assumption of geostrophy (Bryden 1980; Lindstrom and Watts 1994; Phillips and Rintoul 2000; Sévellec et al. 2015). Our study follows in the footsteps of this body of

work, yet applies the density conservation equation to include subinertial ageostrophic flows (see Section 2c).

In this article, we document an annual cycle of the vertical velocity and buoyancy flux (i.e. the rate of restratification by the vertical flow) associated with balanced motions with horizontal scales characteristic of the mesoscale and submesoscale. These diagnostics are based on measurements obtained with a mooring array, deployed in a typical mid-ocean area of the Northeast Atlantic as part of the U.K. OSMOSIS (Ocean Surface Mixing, Ocean Submesoscale Interaction Study) experiment. The outline of the paper is as follows. Data and methods are introduced in Section 2. Section 3 describes the mooring site and outlines the annual cycle of meso- and submesoscale vertical velocities and buoyancy fluxes. Section 4 provides a discussion of the role of mesoscale-driven frontogenesis in forcing submesoscale turbulence. Conclusions are given in Section 5. Appendix A contains a discussion of observational uncertainties. Appendices B-D demonstrate the robustness of our approach to calculating vertical velocity with two numerical models, and with the density conservation equation grounded on the QG framework.

2. Data and Methods

a. Mooring data

Nine bottom-anchored subsurface moorings were deployed over the Porcupine Abyssal Plain (PAP, 48.63-48.75°N, 16.09-16.27°W) site in the Northeast Atlantic Ocean for the period September 2012 – September 2013 (Fig. 1a). The PAP site is an abyssal plain of depth close to 4800 m, and is analogous to many open ocean areas far away from complex topography, where energetic internal waves can be generated.

Coherent mesoscale vortices frequently form in or propagate through this region (Painter et al. 2010; Buckingham et al. 2016; Damerell et al. 2016).

The array, arranged in two concentric quadrilaterals with a centrally located single mooring, is designed to obtain hydrographic and horizontal velocity measurements linked to meso- and submesoscale flows with relatively high (30-100 m) vertical resolution. The four outer moorings were clustered in a 13 km by 13 km box, and thereby resolve mesoscale flows with horizontal scales as small as the local first baroclinic Rossby radius $R_1 = \frac{Nh}{f}$, where h denotes the vertical scale of the main pycnocline, f is the Coriolis frequency, and $N = \sqrt{-\frac{g}{\rho_0} \frac{\partial \rho}{\partial z}}$ is the buoyancy frequency (with g as gravity, ρ as potential density, and $\rho_0 = 1025 \text{ kg m}^{-3}$ as a reference density). Here we will take $h = 800 \text{ m}$, estimated from the local buoyancy e-folding scale. The value of R_1 is in the range of 15-32 km throughout the year, consistent with the result in Chelton et al. (1998). The four inner moorings are clustered more closely, in a 2.5 km by 2.5 km box, and can thus capture submesoscale flows. The ML deformation radius is defined as $R_{ML} = \frac{NH}{f}$ (with H as the ML depth), and lies in the range of 1-4 km with smallest values in summer and largest in winter.

Mooring sensors comprised a series of paired Nortek Aquadopp acoustic current meters (ACMs) and Seabird MicroCAT conductivity-temperature-depth (CTD) sensors at different depths, spanning the approximate depth interval 30-530 m (Fig. 1b). The central mooring is the most heavily instrumented, having 13 CTD/ACM pairs. The inner and outer moorings have seven and five such pairs, respectively. The two nested mooring arrays return temperature, salinity, horizontal velocity and pressure observations at respective horizontal resolutions of approximately 1.5 km and 10 km for the inner and outer moorings. Note that the cross shape of each of the

mooring clusters is well suited to obtaining the lateral gradients of buoyancy and horizontal velocity. Mooring measurements captured most of the pycnocline and ocean interior throughout the year, and most of the ML during the winter months (Fig. 2a). The vertical spacing between CTD/ACM pairs is finer above the base of the deepest winter ML (approximately 300 m, see Fig. 2a) than below; see also Table 1 for detailed information of mooring instruments. In short, ACMs sampled at a frequency of 1 Hz within 1-minute averaging intervals, once in each 10-minute measurement interval. The compass upload was once every second, and the associated heading error was 2°. CTDs sampled continuously for each full 5-minute sampling interval. CTD calibrations were performed before the deployment, and no obvious sign of biofouling was found. The real-time clock in each CTD and ACM had an accuracy of ± 1 min/year; thus clock drift is not expected to influence our results. The accuracy of pressure sensors on CTDs and ACMs was 0.005% of full depth scale, which is 0.24 m at the OSMOSIS site. Moorings were complemented by measurements from two oceanic gliders that navigated in a bow-tie pattern across the mooring array. The present study predominantly uses data from the moored CTD/ACM pairs.

Note that, in this article, our definition of submesoscale refers to subinertial motions of a specific horizontal scale (1-10 km), and thus excludes internal gravity waves and other superinertial phenomena. Previous analyses of our mooring (Buckingham et al. 2016) and glider (Thompson et al. 2016; Erickson and Thompson 2018) observations reveal that these subinertial motions exhibit some of the characteristics of active submesoscale dynamics (McWilliams 2016), e.g., skewness in the vertical component of relative vorticity and occurrence of ML instabilities within and below the base of the ML.

b. Data processing and filtering

We linearly interpolate measurements of temperature, salinity and horizontal velocity onto surfaces of constant depth at 10 m intervals between depths of 50 m and 520 m, and onto uniform 10 minute intervals between 5 September 2012 and 5 September 2013. Potential density (referenced to the ocean surface) and depth are calculated from interpolated temperature, salinity and pressure using the Gibbs Seawater Oceanographic Toolbox (McDougall and Barker 2011). Compressibility effects are considered to be negligible over the top 520 m. These unfiltered versions of data time series, indicated by the subscript ‘*raw*’, are used in spectral analyses (Section 3a). Subsequently, the 10-minute potential density and horizontal velocity data are averaged onto hourly intervals.

Our approach is to distinguish meso- and submesoscale processes, not only by spatial scale as determined by the design of the outer and inner moorings, but also by temporal scale. To do this, we first apply different low-pass filters to outer and inner mooring measurements. Our initial consideration in defining the filter cut-offs is the characteristic advective time scale of each mooring array, i.e. the time typically required for a water parcel to cross the full lateral extent of each array. As the root mean square (RMS) upper-ocean horizontal velocity at the OSMOSIS site is 0.19 m/s, advective time scales of 30 hours and 6 hours may be respectively estimated for the outer and inner mooring domains. All (hourly) potential density and horizontal velocity data from the outer mooring array are low-pass filtered with a fourth-order Butterworth filter (whose power decreases by 24 dB per octave), with a cut-off determined by the outer-array advective time scale (30 hours). In turn, data from the inner mooring array are filtered with a cut-off of one inertial period (16 hours), so as to comply with our definition of submesoscale flows by removing all variability in the

internal wave band. In all calculations of lateral gradients, data from the central mooring are low-pass filtered with the same cut-off as the data from the (outer or inner) mooring array domain from which the gradients are computed.

In the following, we refer to parameters (e.g., vertical velocity or lateral buoyancy gradient) estimated from the outer and inner moorings as *outer* and *inner* quantities, respectively. Outer quantities are representative of meso- and larger-scale flows. In contrast, inner quantities include all dynamically balanced motions with horizontal scales larger than the ML deformation radius R_{ML} and temporal scales longer than one inertial period, including (sub-)mesoscale and larger-scale flows. Unbalanced motions, such as internal tides, near-inertial flows and other high-frequency motions, are removed by the low-pass filtering (16 hours). For simplicity, we use the subscripts 'C', 'I' and 'O' to represent data from the central, inner and outer moorings, respectively. Further, we use the subscripts '16h' and '30h' to denote data filtered over 16 hours and 30 hours, respectively (e.g., $w_{CI,16h}$ denotes vertical velocity calculated from 16-hour low-pass filtered data from the central and inner moorings). Daily-averaged results are denoted as $\langle \cdot \rangle$. A further 30-hour low-pass filter was applied to inner quantities when compared or related to outer quantities in Section 4.

The ML depth is calculated from the glider data using a threshold value of density increase ($\Delta\rho = 0.03 \text{ kg m}^{-3}$) from a near-surface value at 10 m depth (Damerell et al. 2016). The surface heat flux is taken from the ECMWF ERA-Interim reanalysis product (Dee et al. 2011). We ignore the freshwater flux at the OSMOSIS site, since it is negligible compared to the surface heat flux at the OSMOSIS site (Thompson et al. 2016). Geostrophic velocities (u_g, v_g) are obtained from the delayed-time gridded $0.25^\circ \times 0.25^\circ$ AVISO product at the grid points nearest to the OSMOSIS area, and interpolated to the central mooring site.

Finally, the decorrelation time scale is estimated from the e-folding scale of the autocorrelation function. A bootstrap method is employed for confidence interval estimates by randomly sampling 90% of the data 10,000 times and selecting the 250th largest and smallest values.

c. Vertical velocity and buoyancy flux calculation

The density conservation equation is used to determine vertical velocity, neglecting the diffusion term,

$$D_t \rho = \partial_t \rho + u \partial_x \rho + v \partial_y \rho + w \partial_z \rho = 0, \quad (1)$$

where D_t is the material derivative; t is time; u, v, w denote the velocity components in the x, y, z coordinate system; and $\partial_t, \partial_x, \partial_y$ and ∂_z are the temporal, zonal, meridional, and vertical partial derivatives. Note that vertical velocity in the ML is not calculated, as the neglected diffusion term becomes important there. The vertical velocity is estimated from the sum of a local isopycnal displacement term and a horizontal advection term, by rearranging Eq. 1 as

$$w = -\frac{\partial_t \rho}{\partial_z \rho} - \frac{u \partial_x \rho + v \partial_y \rho}{\partial_z \rho}. \quad (2)$$

The first term on the RHS of Eq. 2, defined as

$$w_t = -\frac{\partial_t \rho}{\partial_z \rho}, \quad (3)$$

denotes the Eulerian change in the position of isopycnals and is associated with vertical migration of isopycnals or isopycnal heave. The second term on the RHS of Eq. 2 is the vertical velocity associated with flow along sloping isopycnals, and is defined as

$$w_h = -\frac{u \partial_x \rho + v \partial_y \rho}{\partial_z \rho}. \quad (4)$$

The vertical derivative of ρ (i.e. $\partial_z \rho$) is calculated as a centered finite difference in depth, and used to compute N^2 . The temporal derivative of ρ (i.e. $\partial_t \rho$) is calculated

as a second-order centered finite difference in time. These two terms ($\partial_z \rho$ and $\partial_t \rho$) and horizontal velocity (u and v) are computed from measurements at the central mooring, whereas lateral density gradients ($\partial_x \rho$ and $\partial_y \rho$) are respectively derived from outer and inner mooring measurements for outer and inner vertical velocities ($w_{CO,30h}$ and $w_{CI,16h}$). As indicated in Section 2b, the two components of $w_{CO,30h}$ and $w_{CI,16h}$ can be expressed as $(w_t)_{C,30h}$, $(w_h)_{CO,30h}$ and $(w_t)_{C,16h}$, $(w_h)_{CI,16h}$, respectively. Note that, since superinertial flows are removed by low-pass filtering all density and velocity data, both w and its components (w_t and w_h) exclusively reflect contributions from subinertial flows.

The validity of our method for the estimation of vertical velocity below the ML is demonstrated with the aid of output from an idealized numerical model (Brannigan et al. 2015) in Appendix B. As Bryden (1980) showed that the w_h term can be estimated from the rotation of the horizontal velocity vector with depth by assuming geostrophic balance, we additionally examine this alternative approach to ground-truth our diagnostics of vertical velocity in Appendix C. Further, a direct comparison between mooring-based vertical velocity estimates and modelled vertical velocities from a high-resolution realistic numerical simulation (LLC4320, Su et al. 2018) is shown in Appendix D, to further corroborate the realism of our estimates.

The perturbation vertical buoyancy flux is $w'b'$, where buoyancy b is defined as $b = -\frac{g}{\rho_0}(\rho - \rho_0)$ and the primes denote deviations from the 10-day running mean. This choice of time window is based on the characteristic decorrelation time scales of w and b , which are 3 and 5.2 days, respectively, i.e. of $O(10)$ days. We expect this time window width to be sufficiently short that a spatial average of w and b would not change appreciably over that period. In order to compare the magnitude of outer

and inner restratification with atmospheric forcing, the eddy component of the vertical buoyancy flux can be represented in terms of an equivalent heat flux, defined as,

$$Q_w = w'b' \frac{c_p \rho_0}{\alpha_T g}, \quad (5)$$

where C_p is the specific heat capacity, and α_T is the thermal expansion coefficient of seawater.

d. Frontogenesis function

In the upper ocean, a large-scale confluent flow intensifies lateral buoyancy gradients through frontogenesis. This effect is quantified as

$$D_t(\nabla_h b) = \vec{Q} = (-\partial_x u \partial_x b - \partial_x v \partial_y b, -\partial_y u \partial_x b - \partial_y v \partial_y b), \quad (6)$$

where \vec{Q} is the ‘Q vector’ (Hoskins et al. 1978) and $\nabla_h b = (\partial_x b, \partial_y b)$ is the lateral buoyancy gradient. Following Hoskins (1982), we use the frontogenesis function to diagnose the impact of frontogenesis on the magnitude of lateral buoyancy gradients,

$$Fs = \frac{1}{2} D_t(|\nabla_h b|^2) = \vec{Q} \cdot \nabla_h b. \quad (7)$$

Additionally, we define the current speed as

$$U = \sqrt{u^2 + v^2}, \quad (8)$$

and eddy kinetic energy (EKE) as

$$EKE = \frac{1}{2} (u'^2 + v'^2). \quad (9)$$

This definition is re-expressed as $EKE_g = \frac{1}{2} (u_g^2 + v_g^2)$ when calculating the geostrophic EKE associated with the geostrophic velocity (u_g, v_g) , estimated from AVISO sea surface height data.

e. Rossby and balanced Richardson numbers

Dynamically, submesoscale flows are characterized by Rossby and balanced Richardson numbers of $O(1)$, indicating that the Earth’s rotation is significant but not

dominant in governing the dynamics of the flow (Thomas et al. 2008). Here we define the Rossby number as

$$\text{Ro} = \zeta/f, \quad (10)$$

where $\zeta = \partial_x v - \partial_y u$ is the vertical component of relative vorticity. The balanced Richardson number is defined as

$$\text{Ri}_B = N^2/(\partial U_g/\partial z)^2 = f^2 N^2/|\nabla_h b|^2. \quad (11)$$

f. Definition of seasons

In this work, the conventional definition of seasons is adopted: fall (21 September to 20 December), winter (21 December to 20 March), spring (21 March to 20 June) and summer (21 June to 20 September).

3. Results

a. Annual cycle of upper-ocean hydrography and horizontal flow

The 30-hour low-pass-filtered time series of stratification $N_{C,30h}^2$ and current speed $U_{C,30h}$ at the central mooring are shown in Figs. 2a-b. The ML depth exhibits a significant seasonal cycle, shoaling to less than 30 m during summer and deepening to approximately 300 m during winter. The ocean is generally stratified with a shallow ML above a strongly stratified pycnocline during the fall and summer months (e.g., September and July). This strongly stratified pycnocline inhibits the outcropping of isopycnals from the ocean interior to the ML. During wintertime, unstable stratification (i.e. $N_{C,30h}^2 < 0$) occurs frequently within the ML, indicating the occurrence of gravitational instability. The maximum value of N^2 from mooring measurements is approximately $0.4 \times 10^{-5} \text{ s}^{-2}$ ($N_{C,30h}/f = 18$), occurring

sporadically in the 200-300 m depth range during winter, and $8 \times 10^{-5} \text{ s}^{-2}$ ($N_{C,30h}/f = 82$) at ~110 m outside of winter, illustrating the strong seasonal cycle of upper-ocean stratification at the OSMOSIS site.

Whereas the maximum $U_{C,30h}$ exceeds 0.5 m s^{-1} , the annual-mean velocity magnitude is less than 0.05 m s^{-1} , characteristic of open-ocean regions with a weak mean flow. Intense flows typically coincide with periods of large mooring knock-down (see white blocks in Fig. 2b). The depth-averaged $EKE_{C,30h}$ estimated from the central mooring matches well with EKE_g from AVISO (Fig. 2c), and $EKE_{C,30h}$ peaks at $0.12 \text{ m}^2 \text{ s}^{-2}$ in May, approximately a factor of 4 smaller than values of $\sim 0.5 \text{ m}^2 \text{ s}^{-2}$ observed in the Gulf Stream (Zhai et al. 2008). The mooring-based $EKE_{C,30h}$ exhibits more high-frequency variability than AVISO-based EKE_g , which typically has coarser temporal resolution and smaller magnitude ($EKE_g < 0.05 \text{ m}^2 \text{ s}^{-2}$). Both $EKE_{C,30h}$ and EKE_g show enhanced values in winter and spring, when multiple mesoscale vortices propagate through the mooring array, captured by AVISO sea level anomaly (not shown).

Additional understanding of the physical processes at the OSMOSIS study region can be gained by computing frequency spectra of the observed variables. Spectra of the horizontal velocity u_{raw} and v_{raw} at the central mooring (Figs. 3a-3b) display high-energy peaks at the M2 semi-diurnal tidal frequency and at the inertial frequency f , which make up a large fraction of the unbalanced kinetic energy in the region. Near-inertial flows are visible as a broad peak around f and decrease in magnitude with depth. M2 signals appear as a sharp peak, and have a higher spectral energy density than near-inertial signals. These features are also evident in spectra of potential density ρ_{raw} (Fig. 3c). All spectra exhibit enhanced energy near the surface at temporal scales characteristic of submesoscale flows (i.e. in the time range between

the inertial period and ~ 10 days), consistent with the expected preferential occurrence of submesoscale turbulence near the ocean surface (Klein et al. 2008; Levy et al. 2012).

While the additional variance observed in the submesoscale band might in part arise from near-inertial flows directly generated by local wind forcing or internal wave energy Doppler-shifted to lower frequencies by mesoscale motions, we find that submesoscale subinertial flows are largely in geostrophic balance. This is illustrated by Fig. 4. Assessment of the degree of geostrophy from the inner cluster reveals strong and statistically significant correlations between measurements of the vertical shear terms (i.e. $-\partial_z u$ and $\partial_z v$) and of the horizontal buoyancy gradient terms (i.e. $\frac{1}{f} \partial_y b$ and $\frac{1}{f} \partial_x b$) in the thermal wind balance equations. Geostrophy explains over 56% of the variance (as indicated by R^2 , with R being the correlation coefficient) of subinertial flows at ~ 2 km. These correlations suggest that the inertial to 10-day variance is likely associated with submesoscale motions that are largely in geostrophic balance.

b. Annual cycle of upper-ocean vertical velocity

The time series of outer and inner vertical velocities inferred from the OSMOSIS moorings are displayed in Figs. 5a-c and 6a-c, after smoothing with a 1-day running mean to facilitate inter-comparison. The diagnosed inner vertical velocity, with RMS ($\langle w_{CI,16h} \rangle$) = 38.0 ± 6.9 m/day, is substantially larger than the outer vertical velocity, with RMS ($\langle w_{CO,30h} \rangle$) = 22.5 ± 3.3 m/day. Vertical velocities associated with flows of both horizontal scales are generally larger in magnitude and more variable in winter and spring than in fall and summer. Intense vertical flows are often observed during the passage of eddy features associated with steep isopycnal slopes; vertical

velocities are notably reduced when isopycnals are relatively flat (e.g., in November and July).

The two components of (outer or inner) vertical velocity, w_t and w_h , are comparable in magnitude, but are often oppositely signed (Figs. 5a-5b and 6a-6b). The $\langle (w_t)_{C,30h} \rangle$ and $\langle (w_t)_{C,16h} \rangle$ terms are highly coherent in depth, while the $\langle (w_h)_{CO,30h} \rangle$ and $\langle (w_h)_{CI,16h} \rangle$ terms occasionally change sign with depth (e.g., at the end of April and in August). This additional vertical structure in $\langle (w_h)_{CI,16h} \rangle$ compared to $\langle (w_h)_{CO,30h} \rangle$ may result from the higher vertical resolution of inner cluster measurements, but may in part be attributable to mooring motion.

Annual-mean vertical velocities (Figs. 5d-f and 6d-f) indicate that the site is characterized by weak downwelling of less than 10 m/day, which arises as a small residual of the highly variable vertical flow. Both outer and inner annual-mean vertical velocities are dominated by the horizontal advection term. This result is consistent with the work of Sévellec et al. (2015) in the Southern Ocean, where the time-mean vertical motion in the deep Drake Passage was found to be primarily determined by the horizontal advection term, shaped by the underlying topography via stratified Taylor column dynamics. We have examined the possibility that a similar mechanism is at play in our study area by considering the vertical scale over which stratified Taylor column dynamics may be influential (Huppert 1975), and found that topographic effects are most likely insignificant in the uppermost 500 m (in which our measurements were acquired) of the ~4300 m-deep water column.

c. Annual cycle of vertical buoyancy flux

The time series of outer and inner vertical buoyancy flux ($\langle w'_{CO,30h} b'_{C,30h} \rangle$ and $\langle w'_{CI,16h} b'_{C,16h} \rangle$) are shown in Fig. 7, having been smoothed with a one-day running mean as in the previous subsection. The RMS of these vertical fluxes of buoyancy is

$O(10^{-7} \text{ m}^2 \text{ s}^{-3})$, with peak values of $O(10^{-6} \text{ m}^2 \text{ s}^{-3})$ occurring frequently in winter and spring. These enhanced vertical buoyancy fluxes commonly extend to 500 m depth. Accordingly, $\langle w'_{CO,30h} b'_{C,30h} \rangle$ and $\langle w'_{CI,16h} b'_{C,16h} \rangle$ during winter and spring (i.e. at times in which the vertical velocity is enhanced) dominate restratification of the upper ocean. $\langle w'_{CO,30h} b'_{C,30h} \rangle$ and $\langle w'_{CI,16h} b'_{C,16h} \rangle$ are more intermittent during fall and summer, when they appear to be closely tied to a small number of mesoscale events (e.g., those on 4-9 June or 6-11 August). Note that the picture of a few discrete events of elevated $w'b'$ remains unchanged when the time window has a width longer than 10 days. Recall that our estimates of vertical velocity are founded on the assumption of negligible diffusive mixing below the ML. Since background thermocline mixing (at a rate of $\kappa \approx 3 \times 10^{-5} \text{ m}^2 \text{ s}^{-1}$; Ledwell et al. 1993) would induce a vertical buoyancy flux of $\kappa b_z \approx 3 \times 10^{-5} \text{ m}^2 \text{ s}^{-1} \times 1.3 \times 10^{-5} \text{ s}^{-2} \approx 4 \times 10^{-10} \text{ m}^2 \text{ s}^{-3}$ (where $b_z \approx 1.3 \times 10^{-5} \text{ s}^{-2}$ is a characteristic value measured by our mooring array) that is much smaller than $\langle w'_{CO,30h} b'_{C,30h} \rangle$ and $\langle w'_{CI,16h} b'_{C,16h} \rangle$, our results are consistent with our starting assumption.

To assess the net contribution of the eddy-induced vertical buoyancy fluxes to the local climatological upper-ocean stratification, vertical profiles of the annual-mean (outer and inner) equivalent heat fluxes are computed from Eq. 5, and compared with the destratification induced by the annually integrated atmospheric cooling of the area. The annual-mean outer equivalent heat flux (Fig. 8) is consistently positive and attains a maximum value of approximately 20 W m^{-2} . The amplitude of outer equivalent heat flux decreases gently with depth. In contrast, the annual mean of the inner equivalent heat flux (Fig. 8) is larger and more surface-intensified, reaching 50 W m^{-2} above 250 m. This vertical range coincides with that in which spectra of horizontal velocity and density show elevated energy at submesoscale frequencies

(Fig. 3). Below 250 m, outer and inner equivalent heat fluxes are similar in magnitude and vertical structure. As the annual-mean surface heat flux is approximately -45 W m^{-2} , and so comparable to the annual-mean inner equivalent heat flux, our results suggest that submesoscale flows contribute importantly to upper-ocean restratification, even in relatively quiescent mid-ocean areas such as the OSMOSIS site.

It is also notable that, as was the case for the annual-mean vertical velocity (Figs. 5d-f and 6d-f), the annual-mean vertical buoyancy flux is dominated by the horizontal advection term (Q_{w_h}) at both horizontal scales. By contrast, the annual-mean (Q_{w_t}) term is close to zero. As $\langle (w_t)_{C,30h} \rangle$ and $\langle (w_t)_{C,16h} \rangle$ are aligned orthogonal to isopycnal surfaces, the vertical transport of buoyancy related to this term does not induce net restratification in the long term.

d. Annual cycle of frontogenesis and lateral buoyancy gradients

Using the year-long time series provided by the OSMOSIS moorings, we document the probability distribution function (PDF) of the outer frontogenesis function, $FS_{O,30h}$, in different seasons (Fig. 9a). The dominant feature is the marked asymmetry between frontogenesis (i.e. positive $FS_{O,30h}$) and frontolysis (i.e. negative $FS_{O,30h}$) during winter and spring, when frontogenetic processes are intensified (with $FS_{O,30h}$ exceeding $1 \times 10^{-20} \text{ s}^{-5}$, or $FS_{O,30h}/f^5 = 0.63$) relative to frontolytic processes, albeit for less than 15% of the time. Over 95% of the values of $FS_{O,30h}$ during the fall and summer are in the range of -0.4×10^{-20} to $0.4 \times 10^{-20} \text{ s}^{-5}$ ($FS_{O,30h}/f^5 = 0.25$). The decorrelation time scale of $FS_{O,30h}$ over the annual cycle of measurements is roughly 2 days. Overall, the increase in the probability of observing positive $FS_{O,30h}$ in winter and spring over that in fall and summer suggests the occurrence of a seasonal cycle in the rate of mesoscale frontogenesis in the upper ocean.

Representative winter and spring times series of $FS_{O,30h}$, $|\nabla_h b|_{I,30h}$ and $|\nabla_h b|_{O,30h}$ are shown in Figs. 9b-d. The magnitude of $|\nabla_h b|_{I,30h}$ is generally a factor of 2 larger than that of $|\nabla_h b|_{O,30h}$, with typical values on the order of 10^{-7} s^{-2} . The decorrelation time scale of $|\nabla_h b|_{I,30h}$ is approximately 3 days. High $FS_{O,30h}$ events correspond to inner lateral buoyancy gradients, $|\nabla_h b|_{I,30h}$, that are enhanced to a greater extent than outer lateral buoyancy gradients, $|\nabla_h b|_{O,30h}$.

Positive values of $\langle FS_{O,30h} \rangle$ display a significant positive trend with $\langle |\nabla_h b|_{I,30h} \rangle$, consistent with an active generation of submesoscale fronts (defined as areas of elevated lateral density gradient with horizontal scales of 1-10 km) by mesoscale frontogenesis (Fig. 10). Notably, the vertical extent of the enhancement of $|\nabla_h b|_{I,30h}$ associated with $FS_{O,30h}$ exceeds the ML depth (Figs. 9b-9c). This may reflect the vertical extent of the ageostrophic secondary circulation required to restore thermal wind balance as frontogenesis unfolds (Thomas and Ferrari 2008).

4. Discussion

a. Mechanisms inducing vertical motion and restratification at the OSMOSIS site

In the previous section, the vertical velocity and buoyancy flux associated with submesoscale motions are shown to be substantially larger than those associated with mesoscale flows. We now consider the possible mechanisms underpinning this result.

Both the outer and inner vertical velocities broadly follow the annual cycle of $EKE_{C,30h}$ at the central mooring (Figs. 2c and 11a). Inner vertical velocity is modest at times of weak mesoscale eddy activity (e.g., in July, with an RMS of 11.3 ± 2.0 m/day), but is elevated when energetic mesoscale features propagate through the mooring array (e.g., in February, with an RMS of 40.0 ± 9.7 m/day). We find that

most of the enhanced inner vertical velocity events coincide with large values of $\langle EKE_{C,30h} \rangle$ (Fig. 11b), yielding a statistically significant correlation coefficient between daily $EKE_{C,30h}$ and daily RMS $\langle w_{CI,16h} \rangle$ of 0.66. This suggests that the presence of mesoscale features may play a role in energising submesoscale flows with pronounced vertical velocity signatures. Outer $\langle w_{CO,30h} \rangle$ also exhibits a positive correlation with $\langle EKE_{C,30h} \rangle$, yet its magnitude ($R = 0.44$, $p < 0.001$) is lower than for inner $\langle w_{CI,16h} \rangle$.

One possible mechanism underpinning the intensification of inner w is the sharpening of submesoscale horizontal buoyancy gradients by mesoscale frontogenesis, which would trigger ageostrophic secondary circulations to restore geostrophy. As mentioned in Section 2b, a further 30-hour low-pass filter was applied to inner variables in investigating the relationship between submesoscale turbulence and mesoscale forcing. We find that the RMS of inner $w'_{CI,30h}$ and associated restratification (i.e. positive $w'_{CI,30h}b'_{C,30h}$) exhibit significant positive correlations with the inner lateral buoyancy gradient, $|\nabla_h b|_{I,30h}$, and with the outer frontogenesis function, $FS_{O,30h}$, at each depth (Fig. 12). This is consistent with the predictions of modeling studies on the regulatory role of mesoscale frontogenesis on submesoscale turbulence (Capet et al. 2008b). These positive correlations are shown to be significant by a bootstrap method. Thus, the variability of vertical velocity on horizontal scales of ~ 2 km is surmised to be due primarily to submesoscale (largely) balanced motions rather than unbalanced internal waves.

Frontogenesis has been indicated by numerical simulations to be most pronounced in a thin surface boundary layer, and to decay rapidly below this layer (Lapeyre et al. 2006). Our observational results present a somewhat different picture, in which

mesoscale frontogenetic processes and intensified submesoscale lateral buoyancy gradients are found well beneath the ML, particularly during winter and spring.

The notable vertical penetration of submesoscale flows is illustrated more explicitly by the structure of the Rossby and balanced Richardson numbers calculated from the outer and inner arrays, shown in Fig. 13. The Rossby number is generally surface-intensified, yet decays only gradually with depth. The inner Rossby number, $\zeta_{I,30h}/f$, is in the range of $-0.8 - 0.8$, a factor of 2 larger than the outer Rossby number, $\zeta_{O,30h}/f$. The inner Rossby number remains of order 1 all the way down to 500 m depth, suggesting that intense vertical flows may extend beyond the ML base. This is in accord with numerical studies, which indicate that submesoscale flows on horizontal scales of $O(1 \text{ km})$ are in geostrophic balance to leading order, despite their association with significant ageostrophic motions (Capet et al. 2008b; Brannigan et al. 2015). In such numerical works, it is shown that departures from geostrophic balance at the submesoscale are associated with intense vertical flow. Thus, the coexistence of a dominant geostrophic component to submesoscale motions, elevated Rossby numbers, and intensified vertical velocities conforms to expectations from numerical simulations. Small values (< 5) of the inner balanced Richardson number are often observed below the ML, and indicate that submesoscale processes may be intensified in episodes of strong lateral buoyancy gradients and relatively weak vertical stratification across the ML base during winter and spring. This result is consistent with the findings of Erickson and Thompson (2018), who used the OSMOSIS glider measurements to demonstrate that submesoscale instabilities energized from the surface boundary can extend down to the ocean interior in wintertime, when the upper-ocean pycnocline is weak at the base of the ML. In contrast, the outer balanced

Richardson number consistently and considerably exceeds the inner balanced Richardson number below the ML.

To synthesise the relationship between the generation of upper-ocean submesoscale turbulence and the occurrence of mesoscale frontogenesis in the OSMOSIS area, we conducted an analysis of the relationship of $w'_{CI,30h}$ and $w'_{CI,30h}b'_{C,30h}$ with positive $FS_{O,30h}$ and $|\nabla_h b|_{I,30h}$. Given the depth independence of the relationship, here we only show depth-averaged results in Fig. 14. No obvious relationship is found between frontolysis (i.e. instances of $FS_{O,30h} < 0$) and vertical velocity, so frontolytic scenarios are not considered further here. Inner vertical velocity and buoyancy flux are clearly enhanced when both of $FS_{O,30h}$ and $|\nabla_h b|_{I,30h}$ are elevated. Persistent frontogenesis induced by the mesoscale strain field is common to periods of large submesoscale horizontal buoyancy gradient and enhanced upper-ocean restratification. This is consistent with mesoscale frontogenesis being a regular precursor of restratifying submesoscale instabilities, and thus suggests that it is likely an important mechanism in generating the observed submesoscale turbulence.

b. Effects of instabilities of balanced flows

Mesoscale BCI is a likely contributor to upper-ocean restratification. This is suggested by the frequent occurrence of a reversal with depth (below the ML base down to ~500 m) of the isopycnal potential vorticity gradient (not shown), which is a necessary condition for the development of the instability (Charney and Stern 1962). Below 250 m, our diagnosed outer and inner equivalent heat fluxes exhibit similar patterns, with values approaching 20 W m^{-2} (Fig. 8). This is indicative of the restratifying action of deep-reaching, slowly-evolving mesoscale eddies in the ocean interior.

Submesoscale instabilities have been argued to be active in the ML, where they

can reverse the sign of the equivalent surface heat flux intermittently in the OSMOSIS domain during winter (Thompson et al. 2016). The enhancement of the upper-ocean vertical velocity and buoyancy flux during winter and spring (when upper-ocean stratification is weakest) in our calculations is consistent with this interpretation, as well as with recent simulations of submesoscale BCI (Callies et al. 2016). It is worth emphasizing that submesoscale BCI and mesoscale frontogenesis are not mutually exclusive, and it is likely that upper-ocean restratification involves some combination of both processes. We thus highlight the likely importance of submesoscale BCI in inducing intense vertical motion and restratification in the upper ocean at the OSMOSIS site.

5. Conclusions

The year-long OSMOSIS mooring observations provide an unprecedented long-term data set to assess the phenomenology of submesoscale vertical flow in the context of measurements of mesoscale motions.

Our results indicate that submesoscale motions act to restratify the upper ocean throughout the year, and most intensely in winter and spring. Enhanced submesoscale vertical velocity and buoyancy flux generally occur in the presence of energetic mesoscale features. Submesoscale subinertial motions at horizontal scales of ~ 2 km depart from geostrophy to a greater degree than mesoscale motions with horizontal scales larger than 10 km. Consequently, substantially larger ageostrophic circulations are induced at the submesoscale, in response to strong frontal tendency to restore geostrophy. Persistent frontogenesis induced by the mesoscale strain field is common to periods of intensified submesoscale lateral buoyancy gradient and rapid surface restratification. This is consistent with mesoscale frontogenesis playing a role in

generating the lateral buoyancy fronts that are necessary for the development of submesoscale turbulence. The role of mesoscale frontogenesis in underpinning the enhanced submesoscale turbulence is suggested by the marked increase in submesoscale vertical velocity and buoyancy flux for periods of intensification of submesoscale lateral buoyancy gradient. The net upper-ocean restratification induced by submesoscale motions over the annual cycle is comparable in magnitude to the destratification associated with the annual-mean atmospheric cooling of the area, indicating that submesoscales play an important role in determining the climatological state of the local stratification.

This study provides observational evidence that strong submesoscale ageostrophic motions penetrate down to at least 500 m below the ocean surface, and at least 200 m below the ML base. One could speculate that large vertical velocities might arise from internal waves coupled to balanced motions, at least in part. However, this effect would more likely impact the w_t term, and hence would not affect the net rate of restratification, which is mainly set by the w_h term. Thus, our results fundamentally challenge the widespread view of upper-ocean submesoscale motions being confined to the ML.

Appendix A: Observational uncertainty

The horizontal motion of the moorings is the main source of uncertainty in our calculation of vertical velocity, especially for the inner variables. Unknown variability in the distances between individual moorings introduces uncertainty into $\partial_x \rho$ and $\partial_y \rho$ that is subsequently propagated into derived variables. Following Buckingham et al. (2016), we modeled the inner-mooring distance perturbations associated with mooring motion as a Gaussian white noise process with zero mean and non-zero

variance, estimated from the time integration of differential horizontal currents. We used the stochastic realizations of mooring positions thus obtained in a Monte Carlo approach to quantify the uncertainty in inner vertical velocity (Figs. 6e-f) and associated equivalent heat flux (Fig. 8) introduced by mooring motion. This source of uncertainty is also estimated for the equivalent outer diagnostics.

A secondary limitation of our dataset is related to mooring knock-down, i.e. the pulling downward of a mooring by the drag of water flowing past the mooring (Meinen 2008). In our case, sub-surface mooring knock-down is mainly caused by mesoscale and submesoscale flows, as well as tidal motions. This introduces temporal variability in the vertical positions of the moored instruments, although large vertical excursions are rare (e.g., vertical excursions in excess of 50 m and 100 m occur only in 3.2% and 0.5% of the mooring record, respectively; see Fig. 2b). The magnitude of the mooring knock-down at the OSMOSIS site was much smaller than for a similar mooring deployment in the Southern Ocean (Sévellec et al. 2015). While there were changes in the orientation of the instruments relative to the vertical (i.e., tilt angle), this perturbation was not excessive. The mooring tilt angle estimated from the Aquadopp roll and pitch angles had a year-mean value of 2.7° , with only 1.8% of the mooring record exhibiting tilts over 10° (not shown). The Aquadopps corrected for tilts for tilt angle $<30^\circ$ when computing u and v . Given the modest mooring knock-down and tilt angle, we choose not to apply mooring motion corrections in the present study. The uppermost buoyant spheres resided at a depth of ~ 30 m, where the oscillatory motion of wind waves and swell would have a minimal influence. Further, the ensemble averaging of 60 consecutive 1-Hz samples performed for the ACMs is expected to greatly suppress the effects of mooring motion associated with surface waves.

As the vertical resolution of the measurements is limited, the motion of the instruments introduces uncertainty into our estimates of w . We have assessed the magnitude of this error by re-doing the calculation of vertical velocity with a vertically sub-sampled vertical stratification N^2 at higher and lower resolutions with the aid of the OSMOSIS glider measurements (Thompson et al. 2016), which sampled the water column at 2-4 m vertical resolution throughout the entire year. We find that our diagnostics are weakly sensitive to the vertical resolution of the data. For instance, varying (higher or lower) the vertical resolution by a factor of 2, the ratios of the RMS of the w_{vary} to the original w are 0.64 and 1.15, respectively. Note that a higher vertical resolution would give a higher N^2 , and thus result in a smaller vertical velocity.

Finally, to test the impact of instrumental errors in the computation of vertical velocity, we propagate the measurement uncertainty in Eqs. 2-4. Following Sévellec et al. (2015), we introduce random noise of prescribed amplitude ($\pm 4 \times 10^{-3}$ K for temperature, $\pm 8 \times 10^{-3}$ psu for salinity and ± 0.5 cm s⁻¹ for horizontal velocity) and allow these uncertainties to accumulate in the calculation of w , with confidence intervals computed at the 90% level using the Monte Carlo method. Results suggest that instrumental errors lead to relative uncertainties to the RMS of 1.50% for the w_t term, 2.41% for the w_h term and 6.25 % for the w . Further, the impact of instrumental errors on other diagnostics such as frontogenesis function and Rossby number have also been examined, with results suggesting that instrumental errors lead to negligible uncertainties.

Appendix B: Testing the calculation of vertical velocity with an idealized numerical model

An idealized doubly-periodic numerical model (Brannigan et al. 2015) is employed to investigate the validity of the non-diffusive density equation used to diagnose vertical motion. The model domain is an analogue of an open ocean region like the OSMOSIS mooring site, where the kinetic energy budget is dominated by mesoscale eddies. The model state from a simulation spun up with 4 km horizontal grid resolution is interpolated to a finer resolution of 0.5 km to permit submesoscale instabilities. The model is integrated for 30 days using MITgcm in a hydrostatic configuration, and model outputs are averaged over one inertial period (about 15.9 h) to reduce inertial-gravity wave effects. The model is forced at the surface by wind forcing and a heat flux, but contains no barotropic tides. The surface boundary condition is calculated relative to a uniform zonal 10 m wind speed of 6.3 m s^{-1} to allow eddy-Ekman interactions, and the surface heat flux is a cooling of 75 W m^{-2} . A limitation of the model is that the internal wave field is likely to be modest, due to the relatively coarse vertical and horizontal resolutions and smoothly varying surface forcing.

Fig. 15a shows the surface temperature at the initial state. The RMS values of vertical motion increase continuously during the model run and the largest values of the vertical velocity below the ML depth are of order 10 m day^{-1} . Data at 258 m depth (below the maximum ML depth) are used to validate our vertical flow calculation method.

First, the amplitudes of w_{DE} computed from the non-diffusive density equation (see Eq. 1) are compared to the w_{model} from simulations. To do so, 100 uniformly distributed data points throughout the model domain are chosen (shown as black dots

in Fig. 15a). The density gradients are calculated on a grid analogous to that of the inner mooring cluster. The absolute minima and maxima in the diagnosed and modeled distributions at each time interval are compared in Fig. 15b. Generally, w_{DE} matches w_{model} well, and the correlation coefficient between the amplitudes of w_{DE} and w_{model} is 0.76. The slope of the linear fitting line is 1.41, suggesting it is likely that the non-diffusive density equation slightly overestimates the intensity of vertical flow. The overestimation of vertical velocity by applying mass conservation is likely to result from numerical and explicit diffusion in the model. The horizontal distribution of vertical velocity implied by the non-diffusive density equation is compared to the modeled vertical velocity field (Figs. 15c-15d). The similarities between the two fields suggest that the non-diffusive density equation diagnoses the horizontal distribution of vertical velocity correctly.

Appendix C: Estimation of vertical velocity from individual moorings under the assumption of geostrophic balance

Following Bryden (1980), the w_h term in Eq. 2 can be expressed as the rotation of the horizontal velocity vector with depth by assuming geostrophic balance,

$$w_{h,g} = -\frac{f\rho(v\frac{\partial u}{\partial z} - u\frac{\partial v}{\partial z})}{\partial_z\rho} = -\frac{f\rho U^2\frac{\partial\phi}{\partial z}}{\partial_z\rho}, \quad (A1)$$

where ϕ is the direction of the flow measured anti-clockwise from east, and $w_{h,g}$ is related to horizontal geostrophic advection. This alternative approach is particularly appropriate for reproducing w from a time series of density and horizontal velocity measurements at multiple depth levels from a single mooring. The vertical velocity $\langle w_{g_{CO,30h}} \rangle$ inferred from the central mooring agrees well with $\langle w_{CO,30h} \rangle$ estimated from density equation with best-fit slopes of 0.80 – 1.06 and statistically significant

correlation coefficients of 0.86 ± 0.10 in the 50 - 500 m range (Fig. 16), thereby endorsing our density conservation-based diagnostics. Further, the vertical profile of $w'b'$ estimated from the above method shows a similar structure and magnitude to those of the outer $w'b'$ profile (Fig. 8).

Appendix D: Direct comparison of observational vertical velocity estimates with a realistic model simulation

The output of the most realistic high-resolution model (the LLC4320 simulation, Su et al. 2018; Torres et al. 2018) available for the OSMOSIS area is used here to provide a direct comparison between our mooring-based estimates of w and the modelled w . The LLC4320 simulation was performed using the MITgcm on a global Latitude-Longitude-Cap (LLC) grid with a time length of 14 months from September 10, 2011 to November 15, 2012. The model fully resolves mesoscale eddies and internal waves, and permits submesoscale variability with an unprecedented horizontal grid spacing of $1/48^\circ$. Horizontal wavenumber spectra suggest that the effective resolution of LLC4320 is about 10 km. The model timestep is 25 s, and model variables are stored at hourly intervals. The model is forced by surface flux fields (with a time interval of 6 hours starting in 2011) from the 0.14° ECMWF atmospheric operational model analysis, which include 10-m wind velocity, 2-m air temperature and humidity, downwelling long and shortwave radiation, and atmospheric pressure load. Importantly, the model also includes 16 major tidal constituents that are applied as additional atmospheric pressure forcing.

Fig. 17 demonstrates that vertical velocities in the model are enhanced in winter and penetrate significantly beyond the base of the ML, as in the observations. Further, the features of relatively weak w in the thermocline and enhanced w at depth at times

other than winter from the LLC4320 simulation are also consistent with the variability of mooring-based w estimates. The reason that modelled vertical velocities are somewhat smaller than those in the observations is most likely the limited (submesoscale-permitting, but not -resolving) resolution of the model, as illustrated by the flattening of the spectrum at horizontal wavelengths shorter than 10 km (Fig. 17d).

Acknowledgments. This research was funded by grants from the Natural Environmental Research Council (NE/1019999/1 and NE/101993X/1 as part of the OSMOSIS project). The responses of Baylor Fox-Kemper and four anonymous reviewers have greatly improved the manuscript. We acknowledge helpful discussions with George Nurser, Eleanor Frajka-Williams, Andrew Thompson and Zachary Erickson. We are grateful to the engineers and scientists at NMFSS, captain and crew of the RRS Discovery, RRS James Cook, and R/V Celtic Explorer, and numerous scientists and technicians that helped during deployment and recovery of the moorings/gliders. All data are archived at the British Oceanographic Data Centre.

References

- Boccaletti, G., R. Ferrari, and B. Fox-Kemper, 2007: Mixed layer instabilities and restratification. *J. Phys. Oceanogr.*, **37**, 2228-2250, doi: 10.1175/JPO3101.1.
- Brannigan, L., D. P. Marshall, A. Naveira-Garabato, and A. J. George Nurser, 2015: The seasonal cycle of submesoscale flows. *Ocean Modell.*, **92**, 69-84, doi: 10.1016/j.ocemod.2015.05.002.
- Brannigan, L., 2016: Intense submesoscale upwelling in anticyclonic eddies. *Geophys. Res. Lett.*, **43**, 3360-3369, doi: 10.1002/2016GL067926.

- Bryden, H. L., 1980: Geostrophic Vorticity Balance in Midocean. *J. Geophys. Res.*, **85**, 2825-2828, doi: 10.1029/JC085iC05p02825.
- Buckingham, C. E., and Coauthors, 2016: Seasonality of submesoscale flows in the ocean surface boundary layer. *Geophys. Res. Lett.*, **43**, 2118-2126, doi:10.1002/2016GL068009.
- Callies, J., R. Ferrari, J. M. Klymak, and J. Gula, 2015: Seasonality in submesoscale turbulence. *Nat. Commun.*, **6**, 6862, doi: 10.1038/ncomms7862.
- Callies, J., G. Flierl, R. Ferrari, and B. Fox-Kemper, 2016: The role of mixed-layer instabilities in submesoscale turbulence. *J. Fluid Mech.*, **788**, 5-41, doi: 10.1017/jfm.2015.700.
- Capet, X., J. C. McWilliams, M. J. Molemaker, and A. F. Shchepetkin, 2008a: Mesoscale to submesoscale transition in the California current system. Part I: Flow structure, eddy flux, and observational tests. *J. Phys. Oceanogr.*, **38**, 29-43, doi: 10.1175/2007JPO3671.1.
- Capet, X., J. C. McWilliams, M. J. Molemaker, and A. F. Shchepetkin, 2008b: Mesoscale to submesoscale transition in the California current system. Part II: Frontal processes. *J. Phys. Oceanogr.*, **38**, 44-64, doi: 10.1175/2007JPO3672.1.
- Charney, J. G., and M. E. Stern, 1962: On the stability of internal baroclinic jets in a rotating atmosphere. *Journal of the Atmospheric Sciences*, **19** (2), 159–172, doi: 10.1175/1520-0469(1962)019<0159:OTSOIB>2.0.CO;2.
- Charney, J. G., 1971: Geostrophic Turbulence. *J. Atmos. Sci.*, **28**, 1087-1095, doi: 10.1175/1520-0469(1971)028<1087:GT>2.0.CO;2.
- Chelton, D. B., R. A. de Szoeke, M. G. Schlax, K. E. Naggar, and N. Siwertz, 1998: Geographical variability of the first baroclinic Rossby radius of deformation. *J.*

- Phys. Oceanogr.*, **28**, 433-460, doi: 10.1175/1520-0485(1998)028<0433:GVOTFB>2.0.CO;2.
- Damerell, G. M., K. J. Heywood, A. F. Thompson, U. Binetti, and J. Kaiser (2016), The vertical structure of upper ocean variability at the Porcupine Abyssal Plain during 2012–2013. *J. Geophys. Res.*, **121**, 3075–3089, doi:10.1002/2015JC011423.
- Dee, D. P., and Coauthors, 2011: The ERA-Interim reanalysis: Configuration and performance of the data assimilation system. *Quart. J. Roy. Meteor. Soc.*, **137**, 553–597, doi:10.1002/qj.828.
- Erickson, Z. K., and A. F. Thompson, 2018: The seasonality of physically driven export at submesoscales in the northeast Atlantic Ocean. *Global Biogeochem. Cycles*, **32**, 1144-1162, doi: 10.1029/2018GB005927.
- Fox-Kemper, B., R. Ferrari, and R. Hallberg, 2008: Parameterization of mixed layer eddies. Part I: Theory and diagnosis. *J. Phys. Oceanogr.*, **38**, 1145-1165, doi: 10.1175/2007JPO3792.1.
- Gill, A. E., J. S. A. Green, and A. J. Simmons, 1974: Energy partition in the large-scale ocean circulation and the production of mid-ocean eddies. *Deep-Sea Res. Oceanogr. Abstr.*, **21**, 499–528, doi:10.1016/0011-7471(74)90010-2.
- Gula, J., M. J. Molemaker, and J. C. McWilliams, 2014: Submesoscale Cold Filaments in the Gulf Stream. *J. Phys. Oceanogr.*, **44**, 2617-2643, doi: 10.1175/JPO-D-14-0029.1.
- Haine, T. W. N., and J. Marshall, 1998: Gravitational, symmetric, and baroclinic instability of the ocean mixed layer. *J Phys Oceanogr*, **28**, 634-658, doi: 10.1175/1520-0485(1998)028<0634:GSABIO>2.0.CO;2.
- Hoskins, B. J., and F. P. Brethert, 1972: Atmospheric Frontogenesis Models - Mathematical Formulation and Solution. *J. Atmos. Sci.*, **29**, 11-37.

- Hoskins, B. J., I. Draghici, and H. C. Davies, 1978: A new look at the ω -equation. *Quart. J. Roy. Meteor. Soc.*, **104**, 31-38.
- Hoskins, B. J., 1982: The Mathematical-Theory of Frontogenesis. *Annu. Rev. Fluid Mech.*, **14**, 131-151, doi: 10.1146/annurev.fl.14.010182.001023.
- Huppert, H. E., 1975: Some remarks on the initiation of Taylor columns. *J. Fluid Mech.*, **67**, 397–412, <https://doi.org/10.1017/S0022112075000377>.
- Klein, P., B. L. Hua, G. Lapeyre, X. Capet, S. Le Gentil, and H. Sasaki, 2008: Upper ocean turbulence from high-resolution 3D simulations. *J. Phys. Oceanogr.*, **38**, 1748-1763, doi: 10.1175/2007JPO3773.1.
- Klein, P., and G. Lapeyre, 2009: The Oceanic Vertical Pump Induced by Mesoscale and Submesoscale Turbulence. *Annu. Rev. Mar. Sci.*, **1**, 351-375, doi: 10.1146/annurev.marine.010908.163704.
- Lapeyre, G., P. Klein, and B. L. Hua, 2006: Oceanic restratification forced by surface frontogenesis. *J. Phys. Oceanogr.*, **36**, 1577-1590, doi: 10.1175/JPO2923.1.
- Ledwell, J. R., A. J. Watson, and C. Law, 1993: Evidence for slow mixing across pycline from open-ocean tracer experiment. *Nature*, **364**, 701–703, doi:10.1038/364701a0.
- Levy, M., R. Ferrari, P. J. S. Franks, A. P. Martin, and P. Riviere, 2012: Bringing physics to life at the submesoscale. *Geophys. Res. Lett.*, **39**, L14602, doi: 10.1029/2012GL052756.
- Lindstrom, S. S., and D. R. Watts, 1994: Vertical Motion in the Gulf-Stream near 68-Degrees-W. *J. Phys. Oceanogr.*, **24**, 2321-2333, doi: 10.1175/1520-0485(1994)024<2321:VMITGS>2.0.CO;2.

- Mahadevan, A., and A. Tandon, 2006: An analysis of mechanisms for submesoscale vertical motion at ocean fronts. *Ocean Modell.*, **14**, 241-256, doi: 10.1016/j.ocemod.2006.05.006.
- Mahadevan, A., L. N. Thomas, and A. Tandon, 2008: Comment on "eddy/wind interactions stimulate extraordinary mid-ocean plankton blooms". *Science*, **320**, 448, doi: 10.1126/science.1152111.
- Mahadevan, A., 2016: The Impact of Submesoscale Physics on Primary Productivity of Plankton. *Annu. Rev. Mar. Sci.*, **8**, 161-184, doi: 10.1146/annurev-marine-010814-015912.
- Martin, A. P., and K. J. Richards, 2001: Mechanisms for vertical nutrient transport within a North Atlantic mesoscale eddy. *Deep-Sea Res. II*, **48**, 757-773, doi: 10.1016/S0967-0645(00)00096-5.
- McDougall, T.J. and P.M. Barker, 2011: Getting started with TEOS-10 and the Gibbs Seawater (GSW) Oceanographic Toolbox, 28pp., SCOR/IAPSO WG127, ISBN 978-0-646-55621-5.
- McWilliams, J. C., M. J. Molemaker, and E. I. Olafsdottir, 2009: Linear Fluctuation Growth during Frontogenesis. *J. Phys. Oceanogr.*, **39**, 3111-3129, doi: 10.1175/2009JPO4186.1.
- McWilliams, J. C., 2016: Submesoscale currents in the ocean, *Philos. Trans. R. Soc. London, Ser. A*, **472**, doi:10.1098/rspa.2016.0117.
- Meinen, C. S., 2008: Accuracy in mooring motion temperature corrections. *J. Atmos. Oceanic Technol.*, **25**, 2293-2303, doi: 10.1175/2008JTECHO555.1.
- Mensa, J. A., Z. Garraffo, A. Griffa, T. M. Ozgokmen, A. Haza, and M. Veneziani, 2013: Seasonality of the submesoscale dynamics in the Gulf Stream region. *Ocean Dyn.*, **63**, 923-941, DOI: 10.1007/S10236-013-0633-1.

- Naveira-Garabato, A. C., J. T. Allen, H. Leach, V. H. Strass, and R. T. Pollard, 2001: Mesoscale subduction at the Antarctic Polar Front driven by baroclinic instability. *J. Phys. Oceanogr.*, **31**, 2087-2107, doi:10.1175/1520-0485(2001)031<2087:MSATAP>2.0.CO;2.
- Painter, S. C., R. E. Pidcock, and J. T. Allen, 2010: A mesoscale eddy driving spatial and temporal heterogeneity in the productivity of the euphotic zone of the northeast Atlantic. *Deep-Sea Res. II*, **57**, 1281-1292, doi: 10.1016/j.dsr2.2010.01.005.
- Phillips, H. E., and S. R. Rintoul, 2000: Eddy variability and energetics from direct current measurements in the Antarctic Circumpolar Current south of Australia. *J. Phys. Oceanogr.*, **30**, 3050-3076, doi: 10.1175/1520-0485(2000)030<3050:EVAEFD>2.0.CO;2.
- Pollard, R. T., and L. A. Regier, 1992: Vorticity and Vertical Circulation at an Ocean Front. *J. Phys. Oceanogr.*, **22**, 609-625, doi: 10.1175/1520-0485(1992)022<0609:VAVCAA>2.0.CO;2.
- Ramachandran, S., A. Tandon, and A. Mahadevan, 2014: Enhancement in vertical fluxes at a front by mesoscale-submesoscale coupling. *J. Geophys. Res.*, **119**, 8495-8511, doi: 10.1002/2014JC01021.
- Rosso, I., A. M. Hogg, P. G. Strutton, A. E. Kiss, R. Matear, A. Klocker, and E. van Sebille, 2014: Vertical transport in the ocean due to sub-mesoscale structures: Impacts in the Kerguelen region. *Ocean Modell.*, **80**, 10-23, doi: 10.1016/j.ocemod.2014.05.001.
- Rosso, I., A. M. Hogg, A. E. Kiss, and B. Gayen, 2015: Topographic influence on submesoscale dynamics in the Southern Ocean. *Geophys. Res. Lett.*, **42**, 1139-1147, doi: 10.1002/2014GL062720.

- Sasaki, H., P. Klein, B. Qiu, and Y. Sasai, 2014: Impact of oceanic-scale interactions on the seasonal modulation of ocean dynamics by the atmosphere. *Nat. Commun.*, **5**, 5636, doi: 10.1038/ncomms6636.
- Sévellec, F., A. C. Naveira Garabato, J. A. Brearley, and K. L. Sheen, 2015: Vertical Flow in the Southern Ocean Estimated from Individual Moorings. *J. Phys. Oceanogr.*, **45**, 2209-2220, doi: 10.1175/JPO-D-14-0065.1.
- Shcherbina, A. Y., and Coauthors, 2015: The LatMix summer campaign: Submesoscale stirring in the upper ocean. *Bull. Amer. Meteor. Soc.*, **96**, 1257–1279, <https://doi.org/10.1175/BAMS-D-14-00015.1>.
- Spall, M. A., 1995: Frontogenesis, Subduction, and Cross-Front Exchange at Upper Ocean Fronts. *J. Geophys. Res.*, **100**, 2543-2557, doi: 10.1029/94JC02860.
- Su, Z., J. Wang, P. Klein, A. F. Thompson and D. Menemenlis, 2018: Ocean submesoscales as a key component of the global heat budget. *Nat. Commun.*, **9**, 775, doi: 10.1038/s41467-018-02983-w.
- Taylor, J. R., and R. Ferrari, 2010: Buoyancy and Wind-Driven Convection at Mixed Layer Density Fronts. *J. Phys. Oceanogr.*, **40**, 1222-1242, doi: 10.1175/2010JPO4365.1.
- Thomas, L. N., and P. B. Rhines, 2002: Nonlinear stratified spin-up. *J. Fluid Mech.*, **473**, 211-244, doi: 10.1017/S0022112002002367.
- Thomas, L. N., and C. M. Lee, 2005: Intensification of ocean fronts by down-front winds. *J. Phys. Oceanogr.*, **35**, 1086-1102, doi: 10.1175/JPO2737.1.
- Thomas, L. N., and R. Ferrari, 2008: Friction, Frontogenesis, and the Stratification of the Surface Mixed Layer. *J. Phys. Oceanogr.*, **38**, 2501-2518, doi: 10.1175/2008JPO3797.1.

- Thomas, L. N., and T. M. Joyce, 2010: Subduction on the northern and southern flanks of the Gulf Stream. *J. Phys. Oceanogr.*, **40**, 429-438, doi: 10.1175/2009JPO4187.1.
- Thomas, L. N., C. Lee, and Y. Yoshikawa, 2010: The subpolar Front of the Japan/East Sea. Part II: Inverse method for determining the frontal vertical circulation. *J. Phys. Oceanogr.*, **40**, 3–25, <https://doi.org/10.1175/2009JPO4018.1>.
- Thomas, L. N., J. R. Taylor, R. Ferrari, and T. M. Joyce, 2013: Symmetric instability in the Gulf Stream. *Deep-Sea Res. II*, **91**, 96-110, doi: 10.1016/j.dsr2.2013.02.025.
- Thompson, A. F., A. Lazar, C. Buckingham, A. C. N. Garabato, G. M. Damerell, and K. J. Heywood, 2016: Open-Ocean Submesoscale Motions: A Full Seasonal Cycle of Mixed Layer Instabilities from Gliders. *J. Phys. Oceanogr.*, **46**, 1285-1307, doi: 10.1175/JPO-D-15-0170.1.
- Torres, H. S., Klein, P., Menemenlis, D., Qiu, B., Su, Z., Wang, J., Chen S., and Fu L. L., 2018: Partitioning ocean motions into balanced motions and internal gravity waves: A modeling study in anticipation of future space missions. *J. Geophys. Res.*, **123**, 8084–8105. <https://doi.org/10.1029/2018JC014438>
- Xie, X. H., Y. Cuypers, P. Bouruet-Aubertot, A. Pichon, A. Lourenco, and B. Ferron, 2015: Generation and propagation of internal tides and solitary waves at the shelf edge of the Bay of Biscay. *J. Geophys. Res.*, **120**, 6603-6621, doi: 10.1002/2015JC010827.
- Zhai, X. M., R. J. Greatbatch, and J. D. Kohlmann, 2008: On the seasonal variability of eddy kinetic energy in the Gulf Stream region. *Geophys. Res. Lett.*, **35**, L24609, doi: 10.1029/2008GL036412.

List of Tables

Table 1. Detailed Configuration of the OSMOSIS Moorings

Mooring	Observation period	Longitude, Latitude	Instrument	CTD/ACM pair Depth (m)	Sample Interval (min)
Central	5 Sep 2012 – 5 Sep 2013	48.6875, -16.1875	ACMs,	50, 77, 109, 145, 168, 194, 228, 261, 299, 359, 405, 466, 527	10
			CTDs	50, 77, 110, 144, 159, 193, 226, 262, 297, 349, 401, 460, 514	5
NE-Inner	6 Sep 2012 – 5 Sep 2013	48.6940, -16.1740	ACMs,	55, 120, 163, 231, 304, 358, 530	10
			CTDs	54*, 115, 163, 234, 302, 355, 517	5
NW-Inner	5 Sep 2012 – 5 Sep 2013	48.7000, -16.2060	ACMs,	27, 84, 133, 200, 274, 331, 493	10
			CTDs	30, 85, 133, 203, 273, 327, 490	5
SE-Inner	6 Sep 2012 – 5 Sep 2013	48.6803, -16.1740	ACMs,	40, 91, 147, 218, 288, 345, 510	10
			CTDs	35, 90, 140, 210, 280, 334, 496	5
SW-Inner	5 Sep 2012 – 5 Sep 2013	48.6780 -16.2050	ACMs,	29, 85, 136, 205, 277, 329, 496	10
			CTDs	31, 85, 133, 206, 275, 330, 493	5
NE-Outer	8 Sep 2012 – 4 Sep 2013	48.7480, -16.0945	ACMs,	61, 121, 235, 360, 511	10
			CTDs	63, 123, 236, 358, 522	5
NW-Outer	8 Sep 2012 – 5 Sep 2013	48.7485, -16.2762	ACMs,	58, 117, 233, 359, 534	10
			CTDs	61, 120, 233, 348*, 520	5
SE-Outer	18 Sep 2012 – 4 Sep 2013	48.6290, -16.0990	ACMs,	52, 113, 229, 354, 525	10
			CTDs	55, 113, 228, 352, 516	5
SW-Outer	5 Sep 2012 – 5 Sep 2013	48.6290, -16.2775	ACMs,	43, 104, 220, 347, 521	10
			CTDs	47, 106, 221, 344, 506	5

Table 1. Detailed configuration of the OSMOSIS moorings. * represents data missing due to a sensor problem.

List of Figures

- Fig. 1.** (a) Geographical location of the OSMOSIS mooring array. The European continent is shaded grey, and bathymetry is shown in the colormap on the right. Inset map shows a magnification of the mooring site. The mooring array includes one central mooring (black), four inner moorings (blue) and four outer moorings (dark yellow). (b) Vertical sections of the OSMOSIS array. Current meters are shown as green diamonds, and MicroCAT-CTDs are shown as red squares.
- Fig. 2.** Time series of (a) stratification $N_{C,30h}^2$, (b) current speed $U_{C,30h}$, and (c) eddy kinetic energy $EKE_{C,30h}$ (black) and EKE_g (red) at the central mooring site. The black line in (a) represents the ML depth. Isopycnals are overlaid as black lines at intervals of 0.05 kg m^{-3} in (b), ranging from 26.90 to 27.20 kg m^{-3} . White blocks in (b) indicate time periods with mooring knockdown larger than 50 m . Depths not sampled by the deployed instrumentation in (a-b) are colored in grey.
- Fig. 3.** Frequency spectra of (a) zonal u_{raw} , (b) meridional v_{raw} components of the velocity, and (c) potential density ρ_{raw} at the central mooring as a function of depth. Signals have been linearly detrended. The 10 days, M2 tidal and inertial periods (f) are marked on the upper axis. The 10 days period is also indicated by the black dashed line.
- Fig. 4.** Relation between the vertical shear and horizontal buoyancy gradient terms in the thermal wind balance equation, at depths from 150 to 500 m represented by color. Scatterplots of (a) $\frac{1}{f} \langle \partial_x b_{I,16h} \rangle$ and $\langle \partial_z v_{C,16h} \rangle$, (b) $\frac{1}{f} \langle \partial_y b_{I,16h} \rangle$ and $-\langle \partial_z u_{C,16h} \rangle$. Reference line with slope 1 is indicated in dashed grey. Correlation coefficient R and p -value are given at the bottom right. All fields are from below the ML.
- Fig. 5.** Time series of the daily-averaged outer vertical velocity and its components in m/day , (a) $\langle (w_t)_{C,30h} \rangle$ term, (b) $\langle (w_h)_{CO,30h} \rangle$ term and (c) $\langle w_{CO,30h} \rangle$ at the central mooring. A positive value indicates upwelling. The ML depth is superimposed as a black line. Isopycnals are overlaid as grey dashed lines. Missing values in our calculations are colored in grey. (d-f) show time-mean values of outer vertical velocity corresponding to (a-c).
- Fig. 6.** Same as Fig.5, but for inner vertical velocity. The grey shaded regions in (e) and (f) illustrate the 90% confidence envelope of time-mean vertical velocity, estimated using a Monte Carlo approach.
- Fig.7.** Year-long time series of daily-averaged vertical buoyancy flux at (a) mesoscale (outer) $\langle w'_{CO,30h} b'_{C,30h} \rangle$ and (b) submesoscale (inner) $\langle w'_{CI,16h} b'_{C,16h} \rangle$ from the central mooring. The black line represents the ML depth. Isopycnals are overlaid as grey dashed lines. Missing values are colored in grey.

- Fig. 8.** Vertical profiles of the year-mean equivalent heat flux. The outer and inner results are indicated by the blue and black solid lines, respectively. The equivalent heat flux estimated from Bryden's (1980) method using the central mooring measurements only is shown by the blue dashed line. The shaded regions illustrate the 90% confidence envelope of year-mean results, estimated using a Monte Carlo approach.
- Fig. 9.** (a) Histogram of depth-averaged outer frontogenesis function $FS_{O,30h}$. Representative winter and spring time series of (b) outer frontogenesis function $FS_{O,30h}$, (c) inner lateral buoyancy gradient $|\nabla_h b|_{I,30h}$ and (d) outer lateral buoyancy gradient $|\nabla_h b|_{O,30h}$ at the central mooring site. The black line in (b-d) shows the ML depth. Missing values are colored in grey.
- Fig. 10.** (a) Scatterplot of daily values of outer frontogenesis $\langle FS_{O,30h} \rangle$ against outer and inner lateral buoyancy gradients $\langle |\nabla_h b|_{I,30h} \rangle$. Fields are from below the ML and depth-averaged. (b) Histograms of outer and inner lateral buoyancy gradients, with respective mean values and Normal distribution fits displayed.
- Fig. 11.** (a) Root mean square of vertical velocity at mesoscale (outer) and submesoscale (inner) throughout the year. The standard deviation is shown by the light shades. (b) Daily root mean square of vertical velocity (dots) as a function of EKE. The mean values of RMS of vertical velocity, discretized in $0.01 \text{ m}^2 \text{ s}^{-2}$ EKE bins, for mesoscale (blue) and submesoscale (grey) are given by the circles.
- Fig. 12.** The relationship between (a) RMS of $\langle w'_{CI,30h} \rangle$ and $\langle FS_{O,30h} \rangle$, (b) RMS of $\langle w'_{CI,30h} \rangle$ and $\langle |\nabla_h b|_{I,30h} \rangle$, (c) $\langle w'_{CI,30h} b'_{C,30h} \rangle$ and $\langle FS_{O,30h} \rangle$, (d) $\langle w'_{CI,30h} b'_{C,30h} \rangle$ and $\langle |\nabla_h b|_{I,30h} \rangle$, at depths from 50 to 500 m represented by color.
- Fig. 13.** Time series of (a) outer Rossby number $\zeta_{O,30h}/f$, (b) inner Rossby number $\zeta_{I,30h}/f$, (c) outer Richardson number $f^2 N_{C,30h}^2 / |\nabla_h b|_{O,30h}^2$ and (d) inner Richardson number $f^2 N_{C,30h}^2 / |\nabla_h b|_{I,30h}^2$ at the central mooring. The black line represents the ML depth. Missing values in (a-b) are colored in grey.
- Fig. 14.** Bin-averaged median values of (a) the RMS of $w'_{CI,30h}$, and (b) $w'_{CI,30h} b'_{C,30h}$, as a function of inner lateral buoyancy gradient $|\nabla_h b|_{I,30h}$ and outer frontogenesis function $FS_{O,30h}$. All fields are depth-averaged. Sample numbers in each bin are indicated in text. Sample numbers < 5 are neglected.
- Fig. 15.** (a) Surface temperature anomaly at the initial state of the model simulation. (b) Relationship between the amplitude of the modeled vertical velocity, w_{model} , and that of the vertical motion implied by the density conservation equation, w_{DE} . The amplitudes (minima and maxima) are extracted from each time interval (i.e. every one inertial period) of the model output at 100 data points, shown as black dots in (a). m is the slope of the linear regression with $\pm 95\%$ confidence intervals estimated by a bootstrapping method.

Reference line with slope 1 is indicated in grey. The horizontal distribution of (c) w_{model} and (d) w_{DE} at a depth of 252 m at day 25.44.

Fig. 16. Comparison of diagnosed $\langle w_{CO,30h} \rangle$ estimated from the density equation and $\langle w_{g_{C,30h}} \rangle$ estimated from the central mooring measurements only as illustrated in Appendix C, at depths from 50 to 500 m represented by color. Reference line with slope 1 is indicated in dashed grey.

Fig. 17. Year-long RMS of vertical velocity (a) averaged over the OSMOSIS region in the LLC4320 simulation, at (b) submesoscale and (c) mesoscale from the central mooring site. (d) Power spectral density (as a function of horizontal wavenumber) of LLC4320 w over 47-49°N, 15-17°W at 40 m depth in winter.

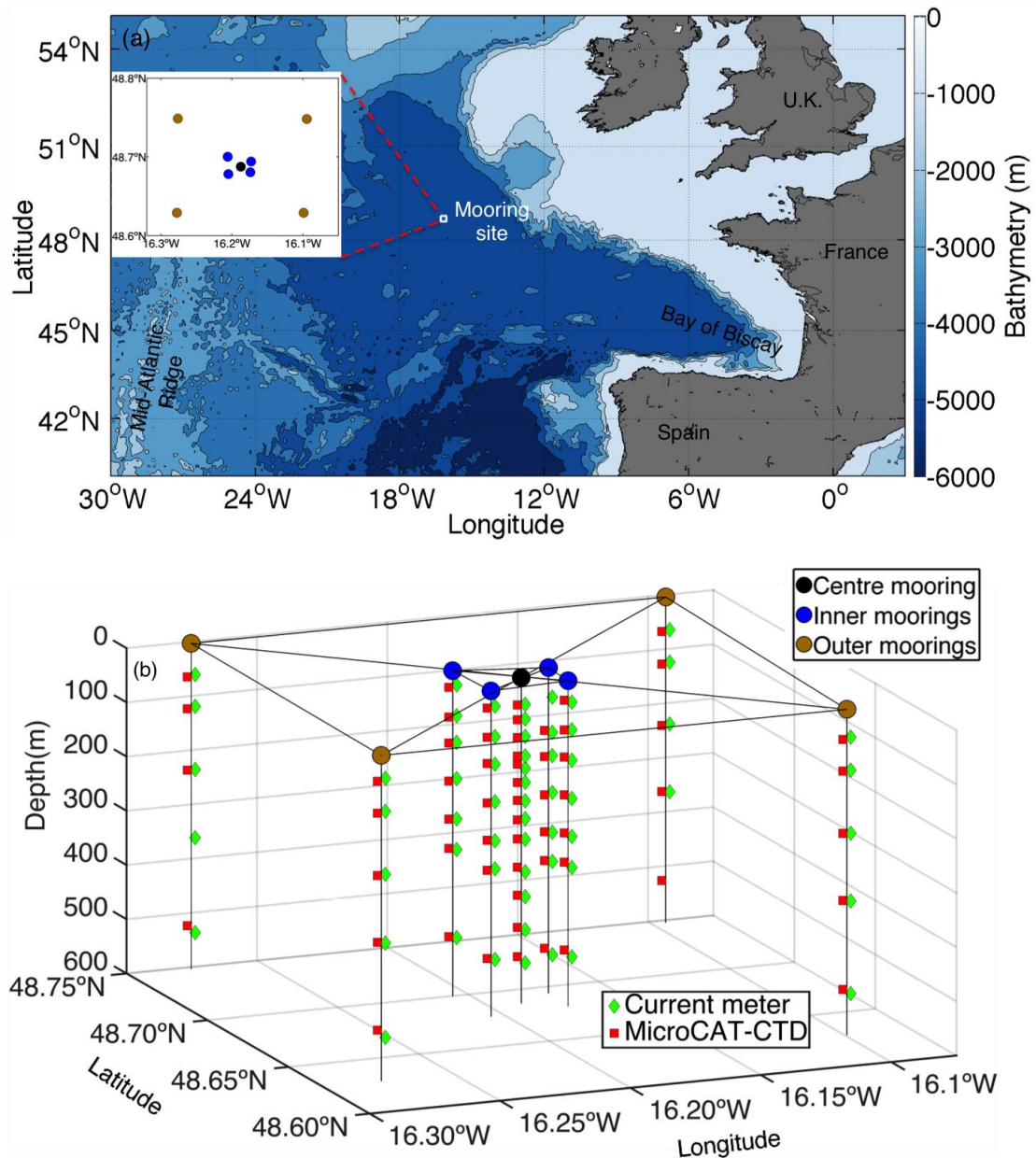


FIG. 1. (a) Geographical location of the OSMOSIS mooring array. The European continent is shaded grey, and bathymetry is shown in the colormap on the right. Inset map shows a magnification of the mooring site. The mooring array includes one central mooring (black), four inner moorings (blue) and four outer moorings (dark yellow). (b) Vertical sections of the OSMOSIS array. Current meters are shown as green diamonds, and MicroCAT-CTDs are shown as red squares.

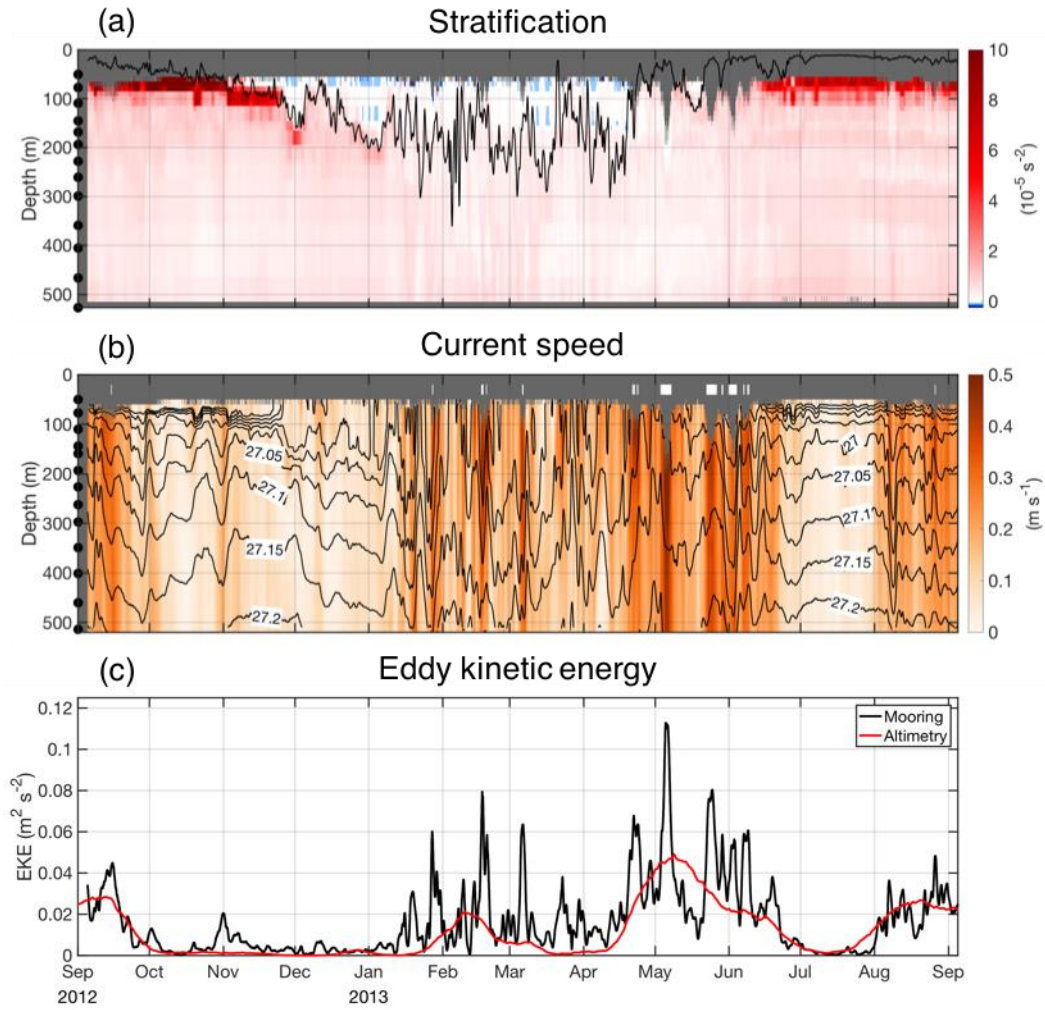


FIG. 2. Time series of (a) stratification $N_{C,30h}^2$, (b) current speed $U_{C,30h}$, and (c) eddy kinetic energy $EKE_{C,30h}$ (black) and EKE_g (red) at the central mooring site. The black line in (a) represents the ML depth. Isopycnals are overlaid as black lines at intervals of 0.05 kg m^{-3} in (b), ranging from 26.90 to 27.20 kg m^{-3} . White blocks in (b) indicate time periods with mooring knockdown larger than 50 m . Depths not sampled by the deployed instrumentation in (a-b) are colored in grey.

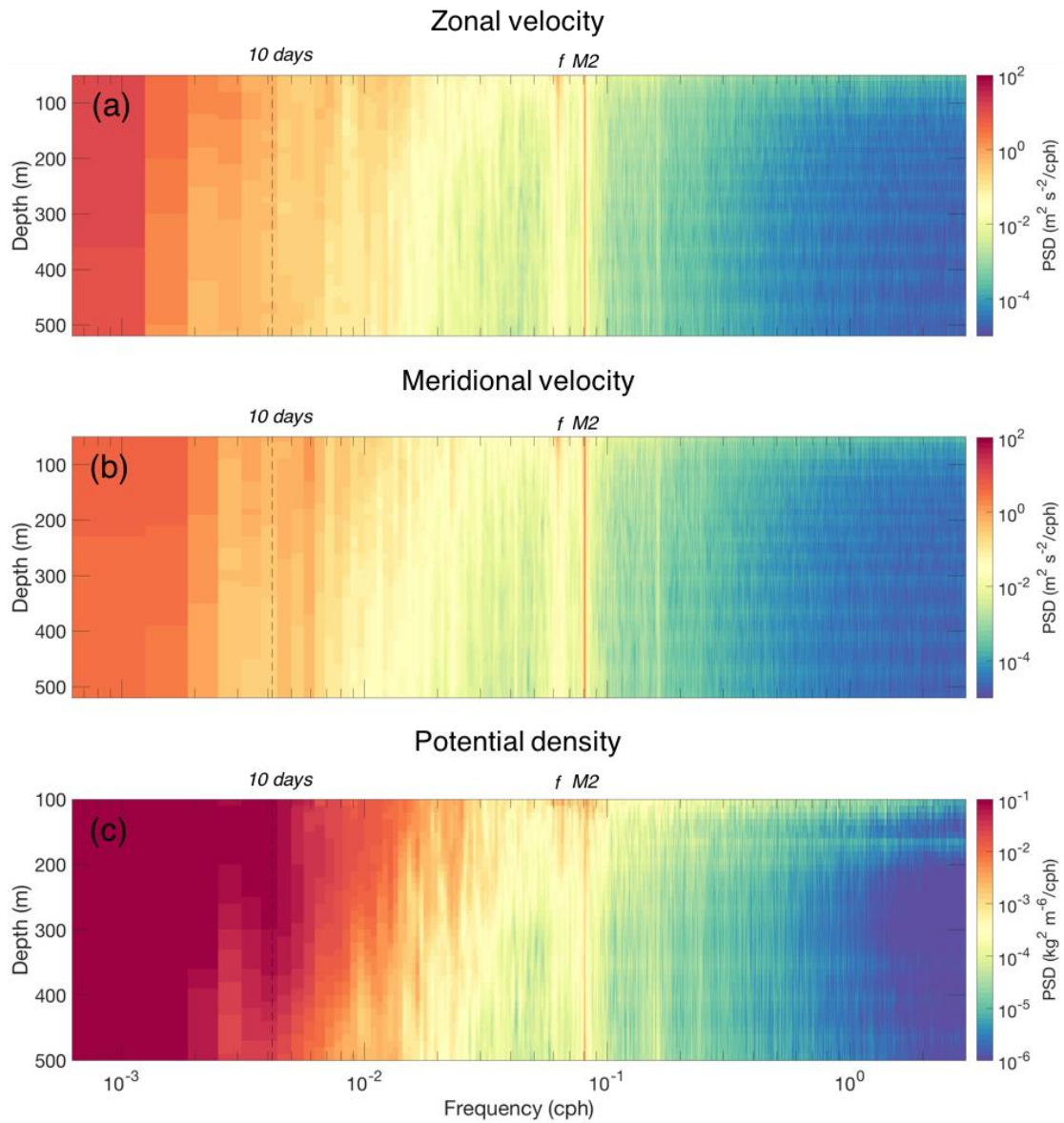


FIG. 3. Frequency spectra of (a) zonal u_{raw} , (b) meridional v_{raw} components of the velocity, and (c) potential density ρ_{raw} at the central mooring as a function of depth. Signals have been linearly detrended. The 10 days, M2 tidal and inertial periods (f) are marked on the upper axis. The 10 days period is also indicated by the black dashed line.

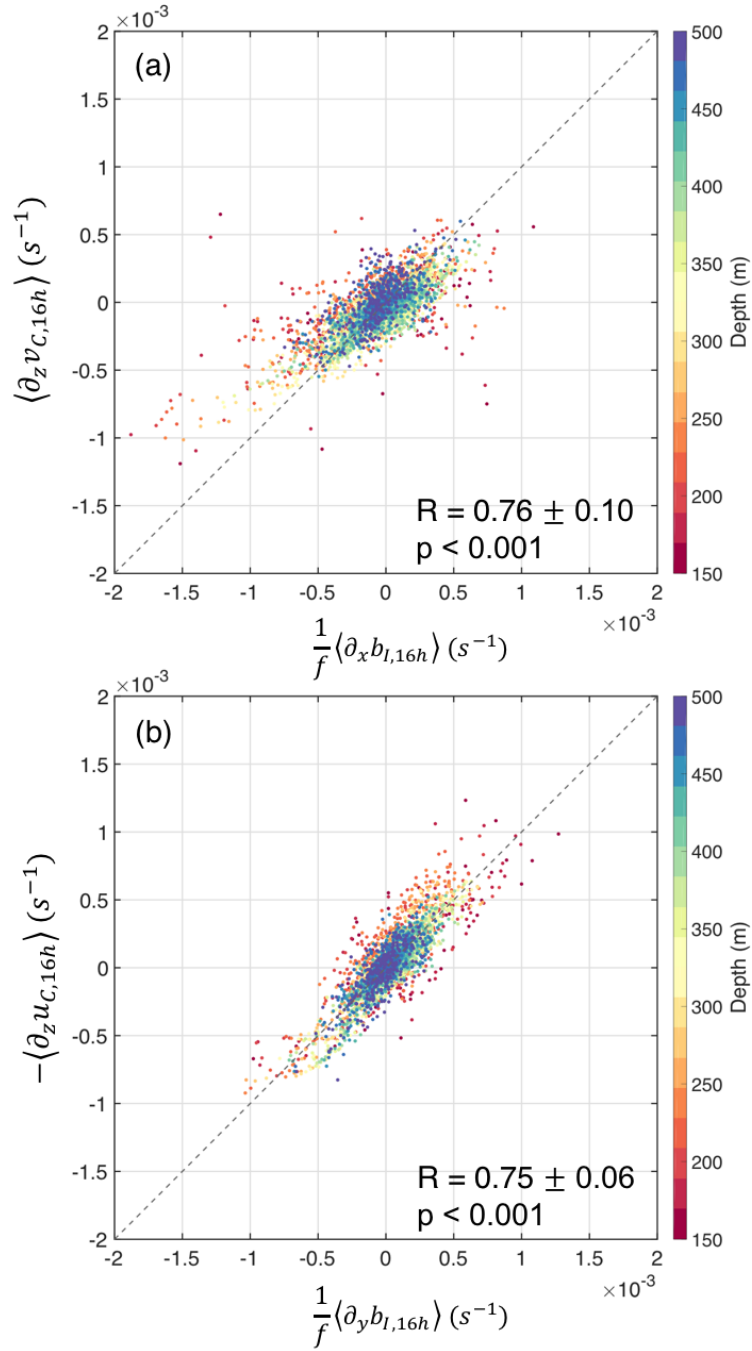


FIG. 4. Relation between the vertical shear terms and horizontal buoyancy gradient terms in the thermal wind balance equation, at depths from 150 to 500 m represented by color. Scatterplots of (a) $\frac{1}{f} \langle \partial_x b_{l,16h} \rangle$ and $\langle \partial_z v_{C,16h} \rangle$, (b) $\frac{1}{f} \langle \partial_y b_{l,16h} \rangle$ and $-\langle \partial_z u_{C,16h} \rangle$. Reference line with slope 1 is indicated in dashed grey. Correlation coefficient R and p -value are given at the bottom right. All fields are from below the ML.

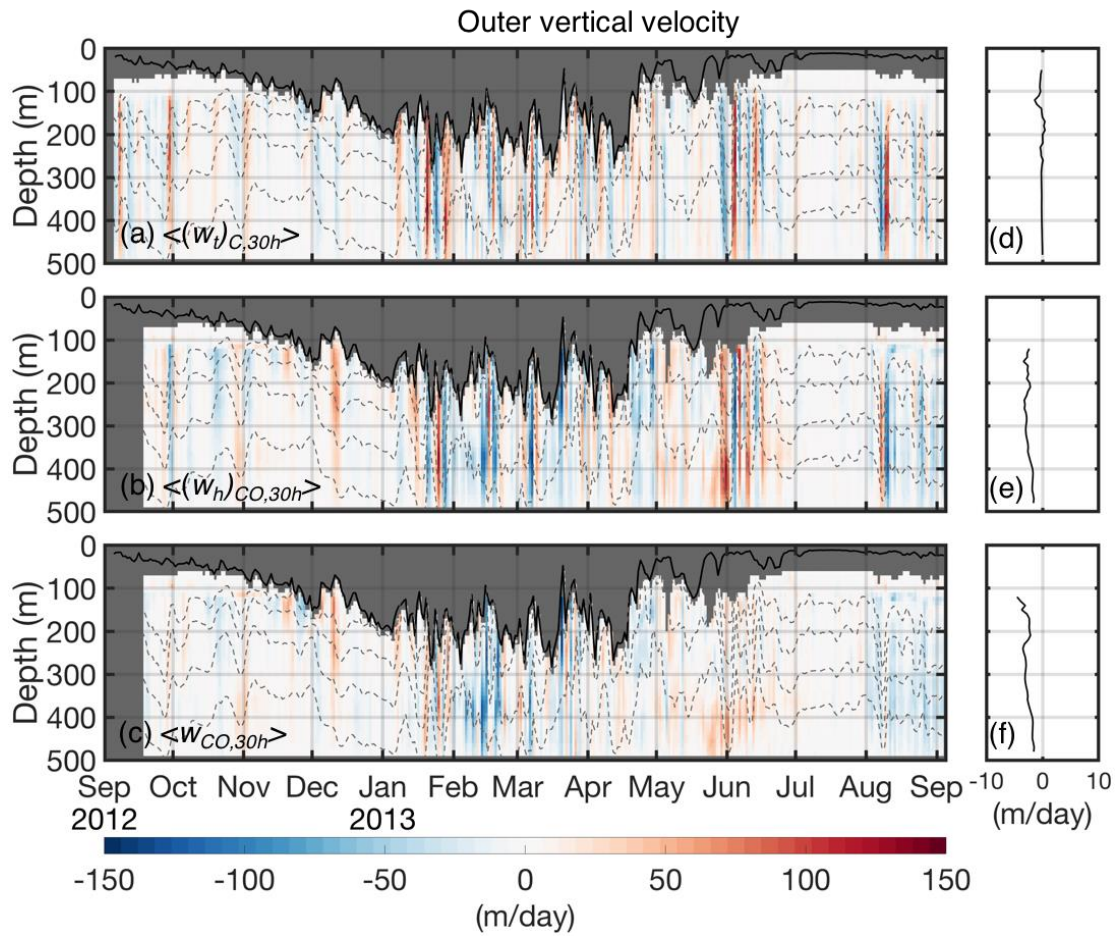


FIG. 5. Time series of the daily-averaged outer vertical velocity and its components in m/day, (a) $\langle (w_t)_{C,30h} \rangle$ term, (b) $\langle (w_h)_{CO,30h} \rangle$ term and (c) $\langle w_{CO,30h} \rangle$ at the central mooring. A positive value indicates upwelling. The ML depth is superimposed as a black line. Isopycnals are overlaid as grey dashed lines. Missing values in our calculations are colored in grey. (d-f) show time-mean values of outer vertical velocity corresponding to (a-c).

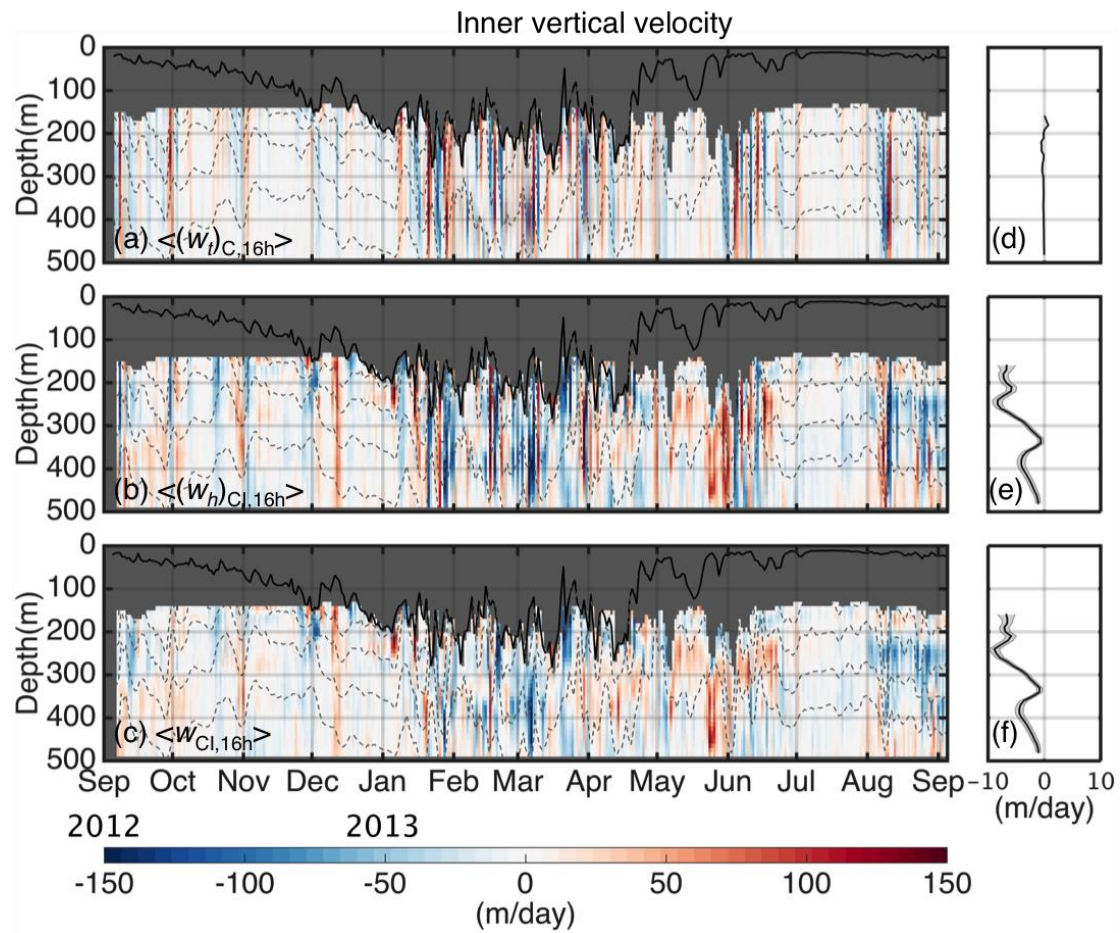


FIG. 6. Same as Fig.5, but for inner vertical velocity. The grey shaded regions in (e) and (f) illustrate the 90% confidence envelope of time-mean vertical velocity, estimated using a Monte Carlo approach.

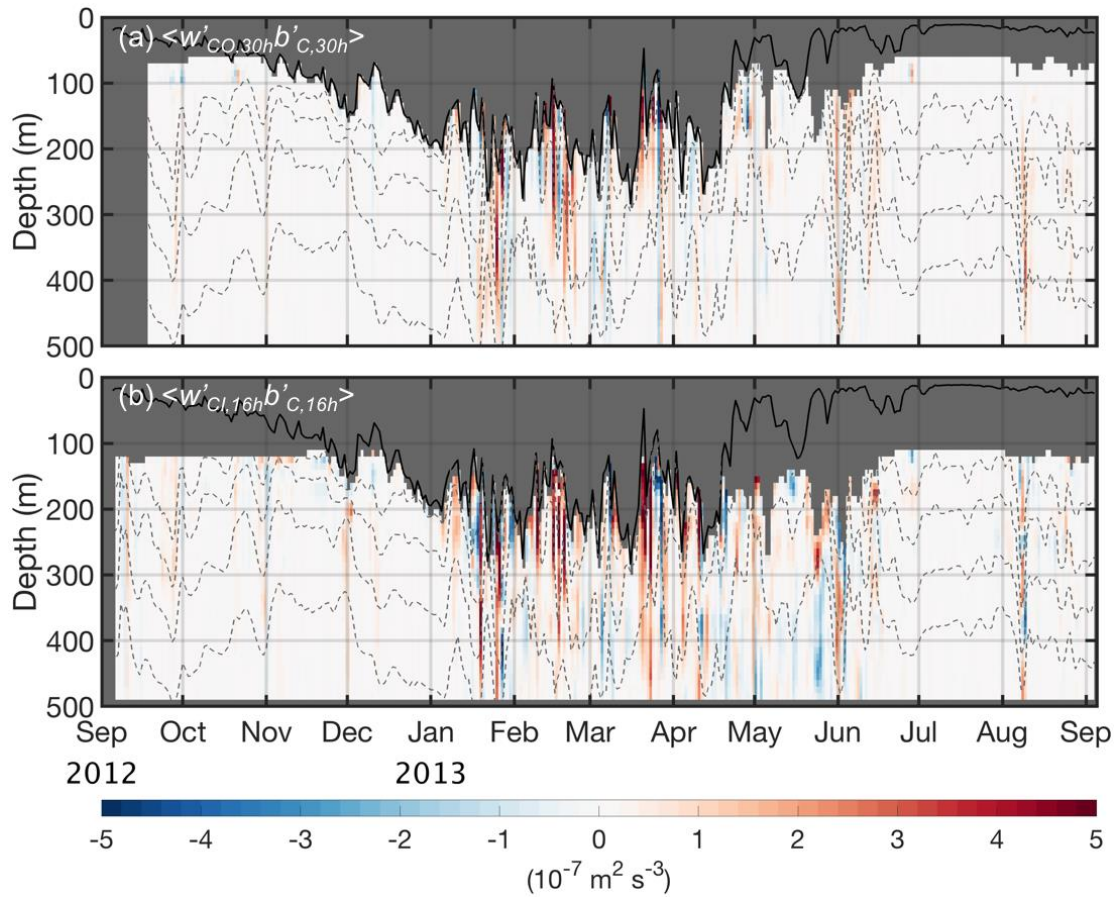


FIG. 7. Year-long time series of daily-averaged vertical buoyancy flux at (a) mesoscale (outer) $\langle w'_{CO,30h} b'_{C,30h} \rangle$ and (b) submesoscale (inner) $\langle w'_{CI,16h} b'_{C,16h} \rangle$ from the central mooring. The black line represents the ML depth. Isopycnals are overlaid as grey dashed lines. Missing values are colored in grey.

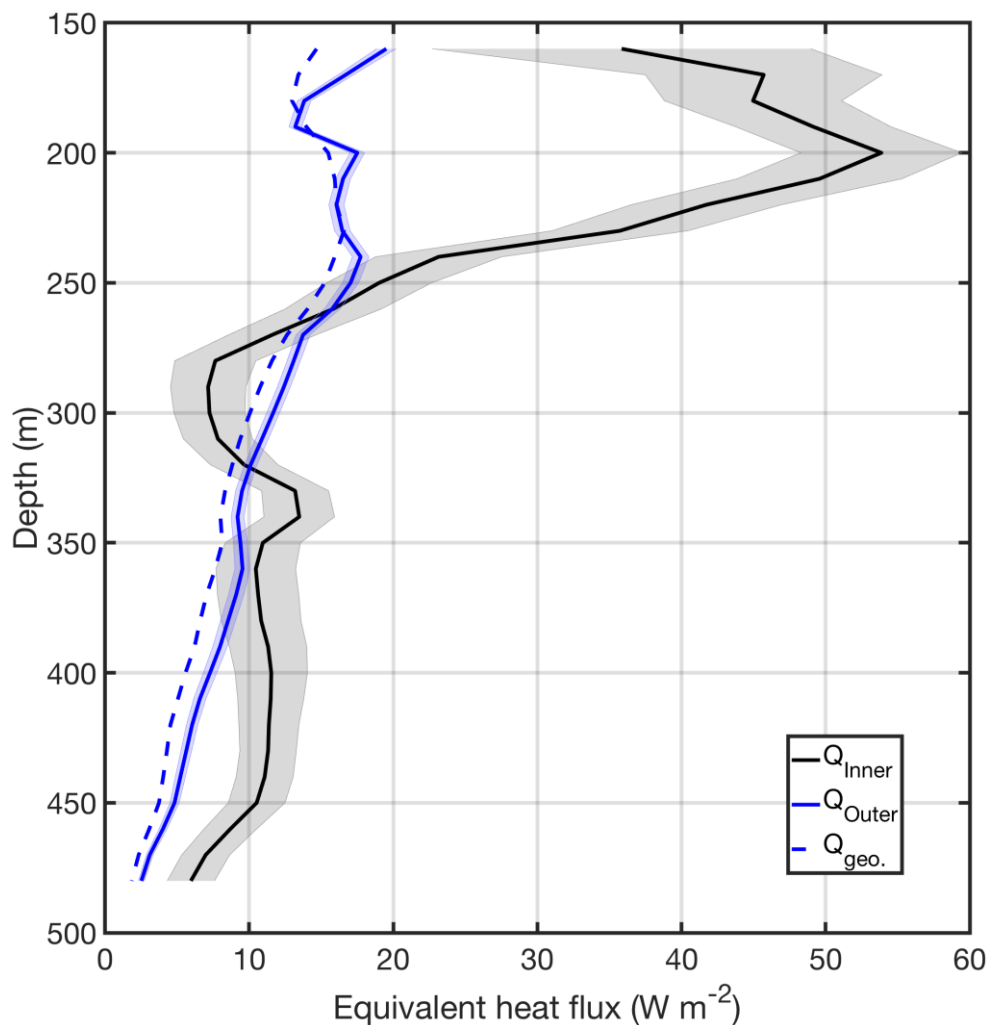


FIG. 8. Vertical profiles of the year-mean equivalent heat flux. The outer and inner results are indicated by the blue and black solid lines, respectively. The equivalent heat flux estimated from Bryden's (1980) method using the central mooring measurements only is shown by the blue dashed line. The shaded regions illustrate the 90% confidence envelope of year-mean results, estimated using a Monte Carlo approach.

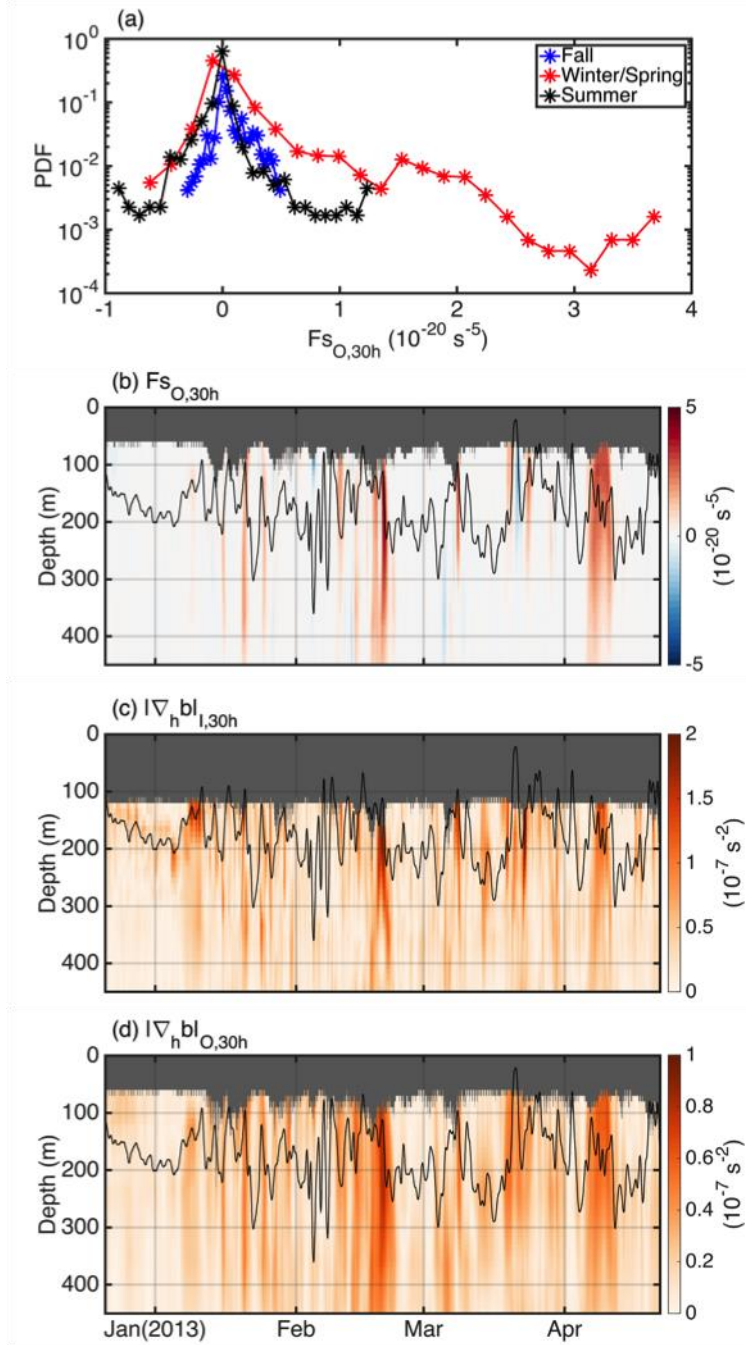


FIG. 9. (a) Histogram of depth-averaged outer frontogenesis function $FS_{O,30h}$. Representative winter and spring time series of (b) outer frontogenesis function $FS_{O,30h}$, (c) inner lateral buoyancy gradient $|\nabla_h b|_{I,30h}$ and (d) outer lateral buoyancy gradient $|\nabla_h b|_{O,30h}$ at the central mooring site. The black line in (b-d) shows the ML depth. Missing values are colored in grey.

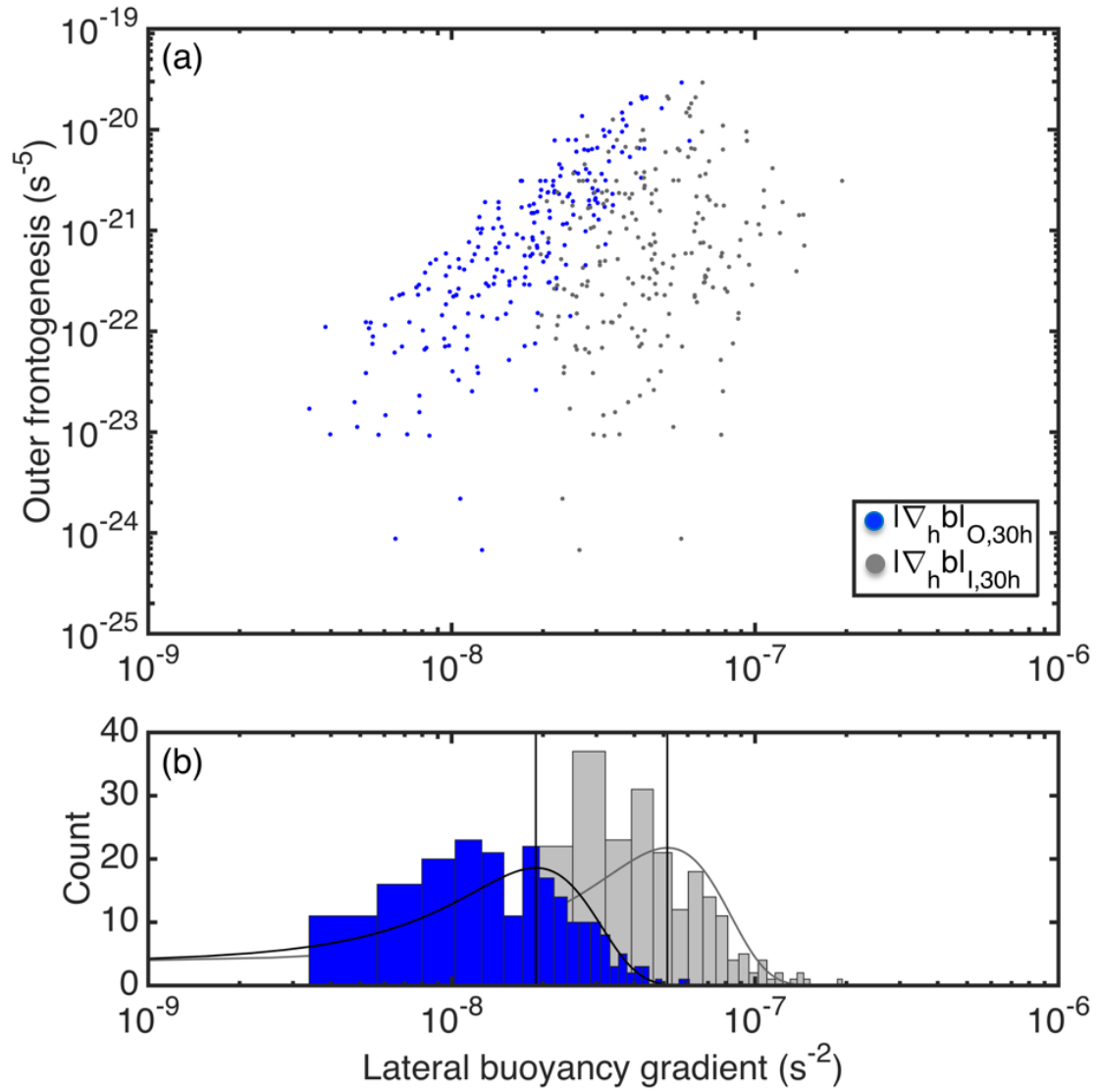


FIG. 10. (a) Scatterplot of daily values of outer frontogenesis $\langle Fs_{O,30h} \rangle$ against outer and inner lateral buoyancy gradients $\langle |\nabla_h b|_{I,30h} \rangle$. Fields are from below the ML and depth-averaged. (b) Histograms of outer and inner lateral buoyancy gradients, with respective mean values and Normal distribution fits displayed.

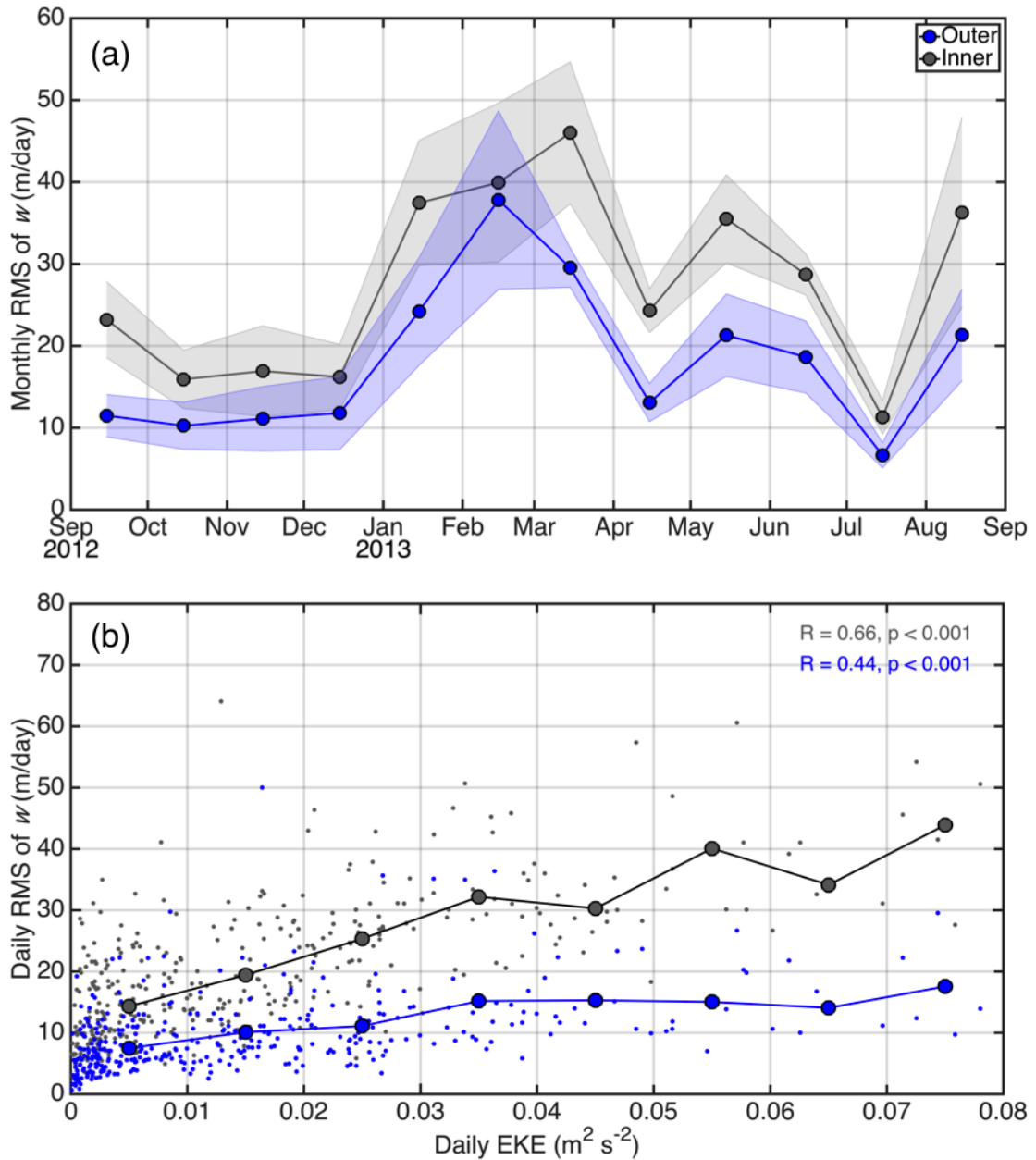


FIG. 11. (a) Monthly RMS of vertical velocity at mesoscale (outer) and submesoscale (inner) throughout the year. The standard deviation is shown by the light shades. (b) Daily RMS of vertical velocity (dots) as a function of EKE. The mean values of RMS of vertical velocity, discretized in $0.01 \text{ m}^2 \text{ s}^{-2}$ EKE bins, for mesoscale (blue) and submesoscale (grey) are given by the circles.

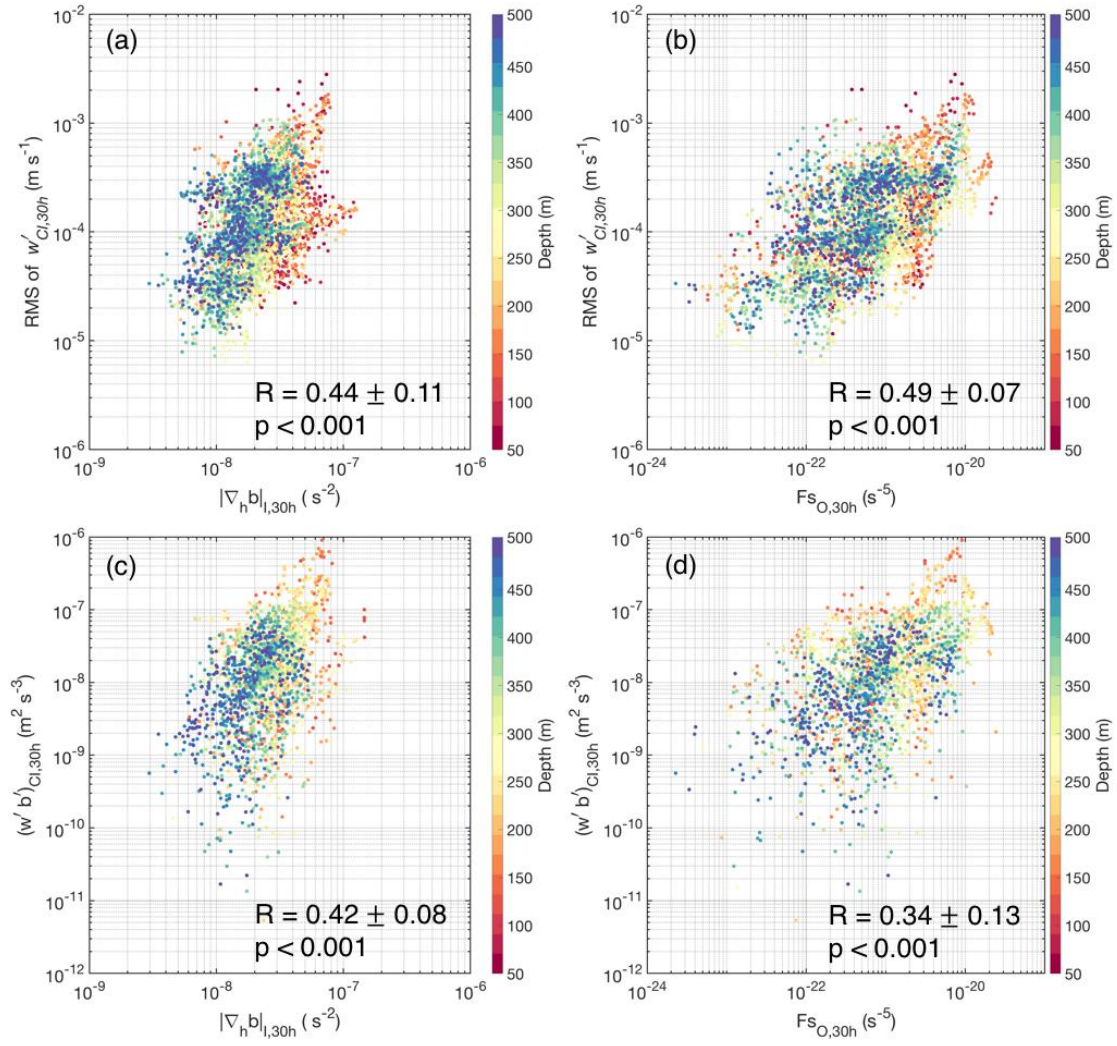


FIG. 12. The relationship between (a) RMS of $\langle w'_{Cl,30h} \rangle$ and $\langle FS_{O,30h} \rangle$, (b) RMS of $\langle w'_{Cl,30h} \rangle$ and $\langle |\nabla_h b|_{l,30h} \rangle$, (c) $\langle w'_{Cl,30h} b'_{C,30h} \rangle$ and $\langle FS_{O,30h} \rangle$, (d) $\langle w'_{Cl,30h} b'_{C,30h} \rangle$ and $\langle |\nabla_h b|_{l,30h} \rangle$, at depths from 50 to 500 m represented by color.

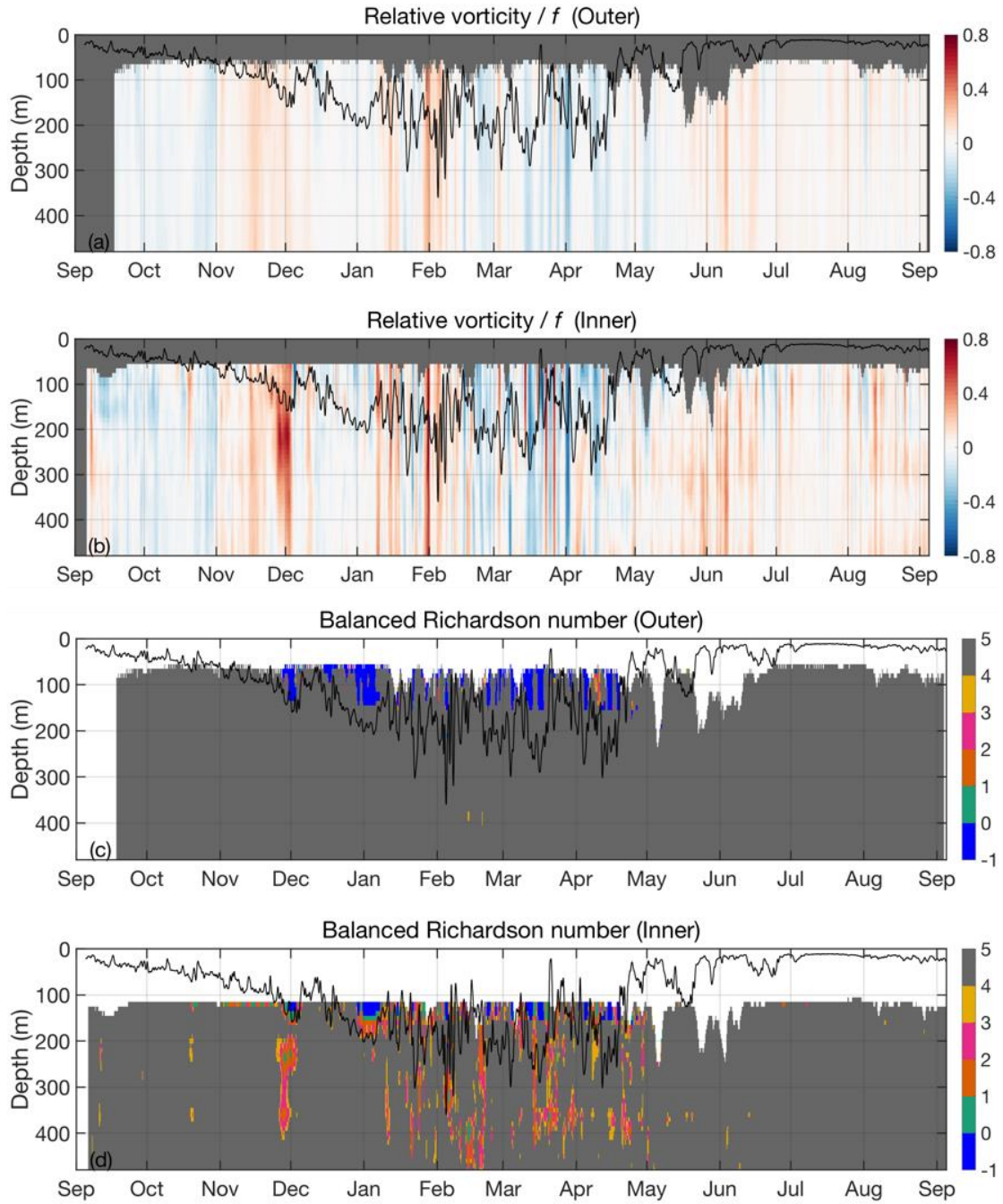


FIG. 13. Time series of (a) outer Rossby number $\zeta_{O,30h}/f$, (b) inner Rossby number $\zeta_{I,30h}/f$, (c) outer Richardson number $f^2 N_{C,30h}^2 / |\nabla_h b|_{O,30h}^2$ and (d) inner Richardson number $f^2 N_{C,30h}^2 / |\nabla_h b|_{I,30h}^2$ at the central mooring. The black line represents the ML depth. Missing values in (a-b) are colored in grey.

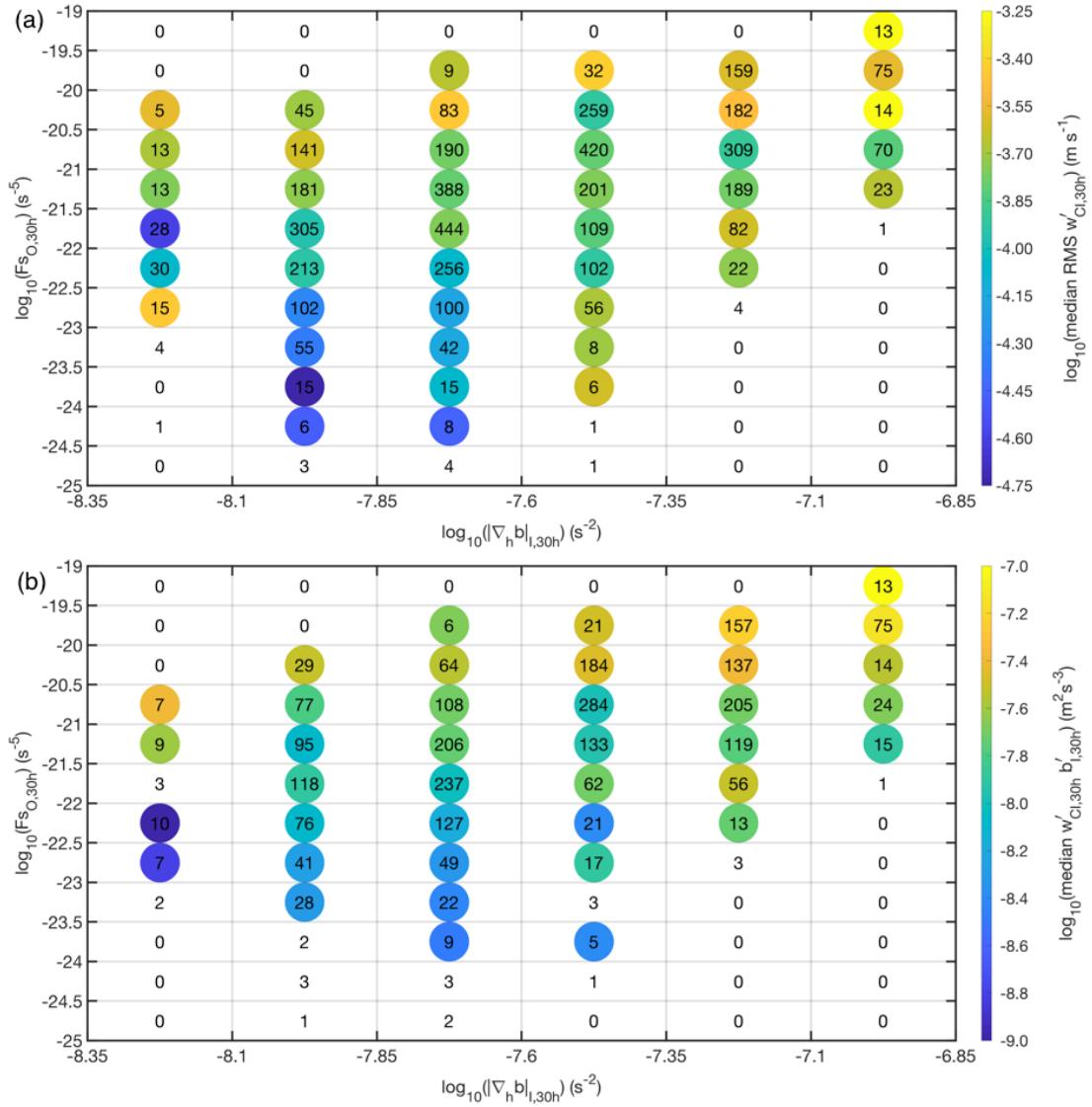


FIG. 14. Bin-averaged median values of (a) the RMS of $w'_{CI,30h}$, and (b) $w'_{CI,30h} b'_{C,30h}$, as a function of inner lateral buoyancy gradient $|\nabla_h b|_{l,30h}$ and outer frontogenesis function $FS_{O,30h}$. All fields are depth-averaged. Sample numbers in each bin are indicated in text. Sample numbers < 5 are neglected.

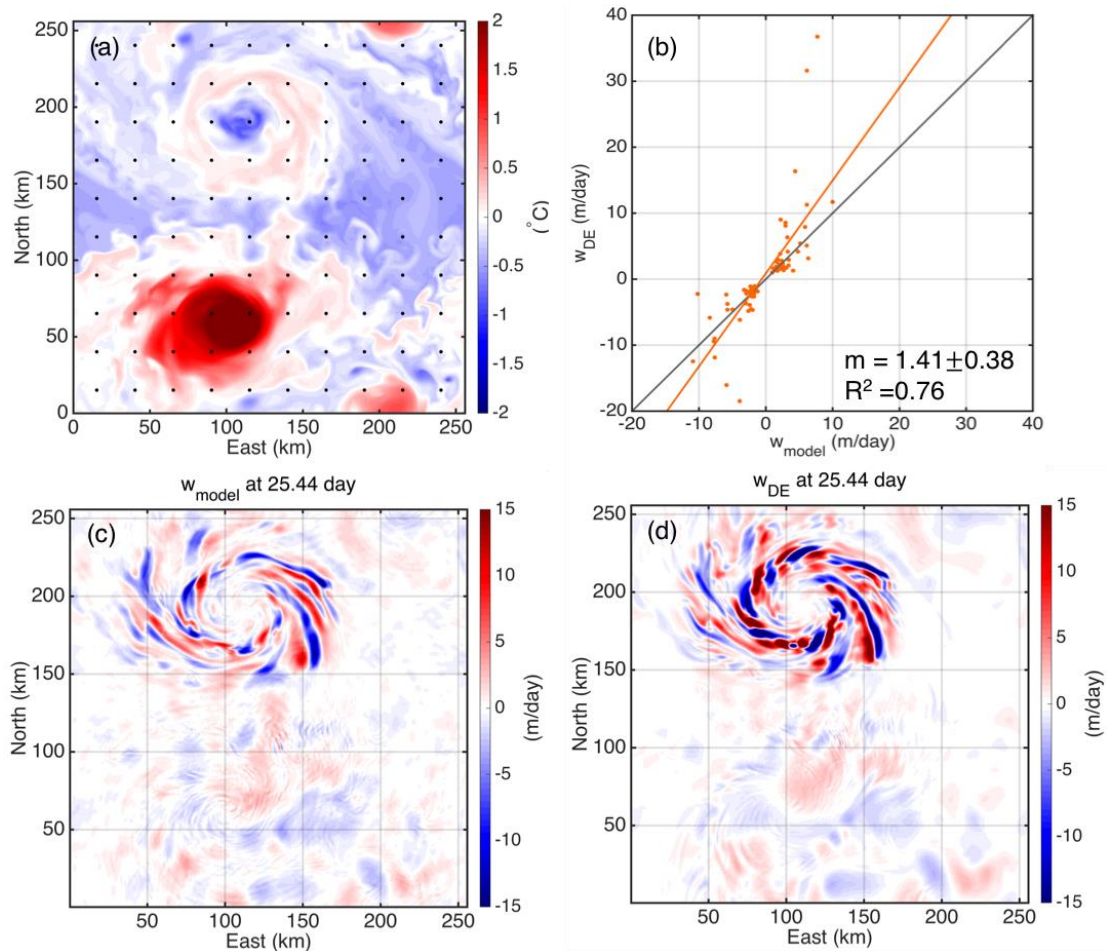


FIG. 15. (a) Surface temperature anomaly at the initial state of the model simulation. (b) Relationship between the amplitude of the modeled vertical velocity, w_{model} , and that of the vertical motion implied by the density conservation equation, w_{DE} . The amplitudes (minima and maxima) are extracted from each time interval (i.e. every one inertial period) of the model output at 100 data points, shown as black dots in (a). m is the slope of the linear regression with $\pm 95\%$ confidence intervals estimated by a bootstrapping method. Reference line with slope 1 is indicated in grey. The horizontal distribution of (c) w_{model} and (d) w_{DE} at a depth of 252 m at day 25.44.

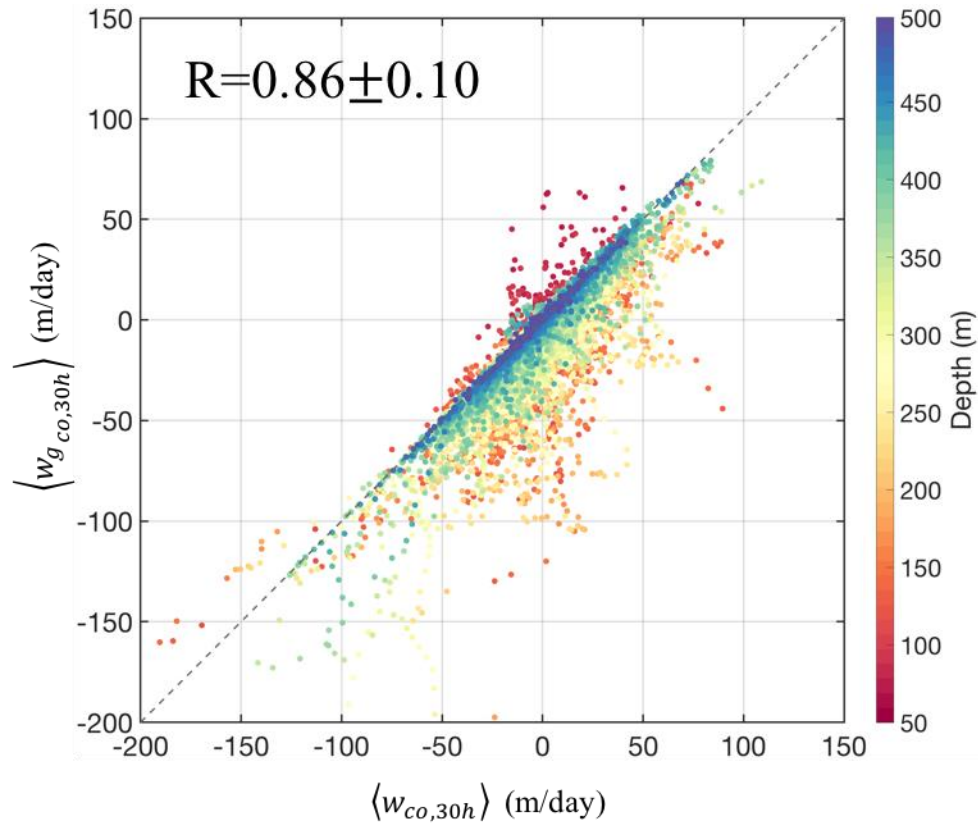


FIG. 16. Comparison of diagnosed $\langle w_{CO,30h} \rangle$ estimated from the density equation and $\langle w_{g,C,30h} \rangle$ estimated from the central mooring measurements only as illustrated in Appendix C, at depths from 50 to 500 m represented by color. Reference line with slope 1 is indicated in dashed grey.

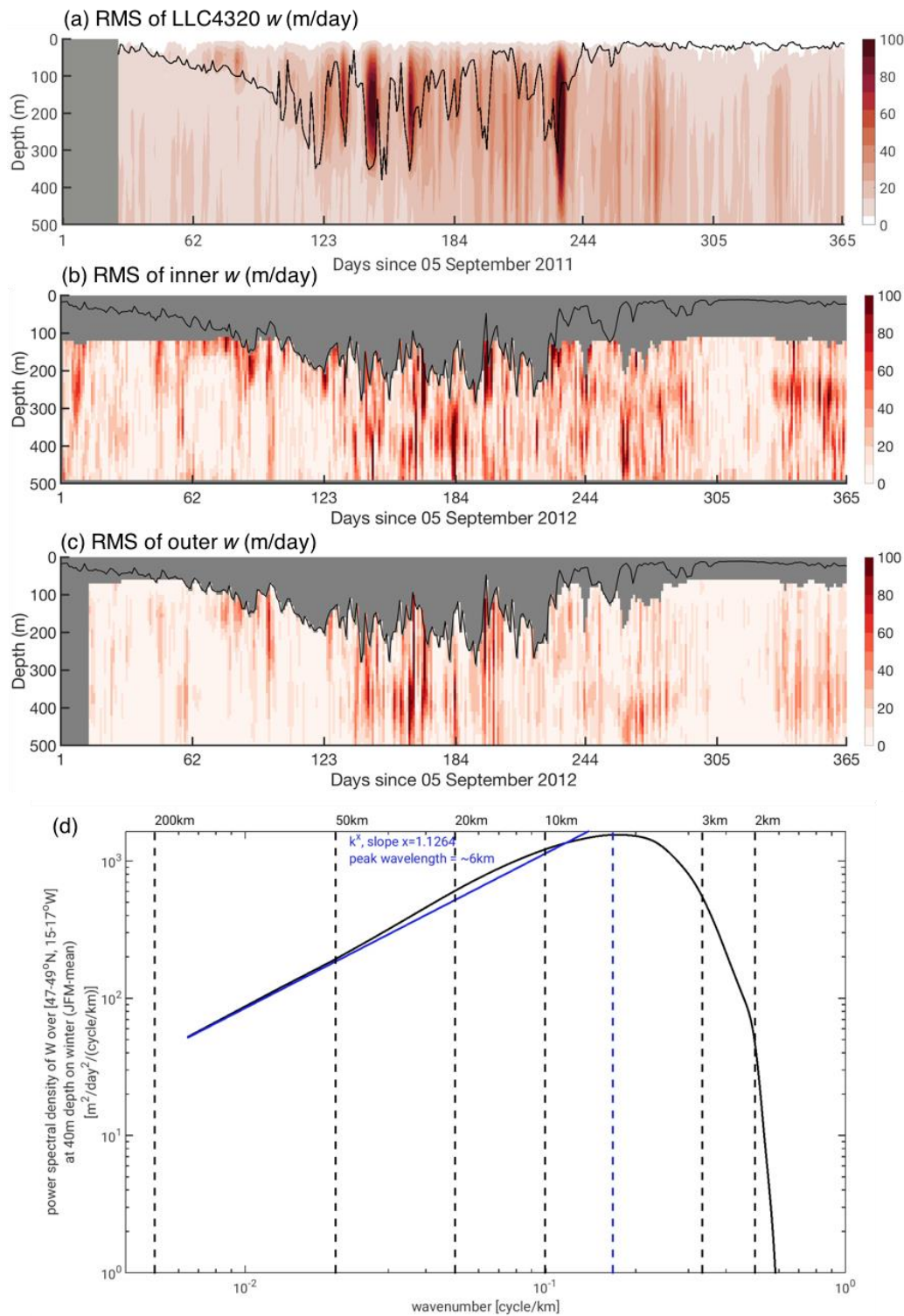


FIG. 17. Year-long RMS of vertical velocity (a) averaged over the OSMOSIS region in the LLC4320 simulation, at (b) submesoscale and (c) mesoscale from the central mooring site. (d) Power spectral density (as a function of horizontal wavenumber) of LLC4320 w over 47-49°N, 15-17°W at 40 m depth in winter.